Correspondence: Dr. Alan M. Jones
Address: Department of Biology
The University of North Carolina at Chapel Hill
Coker Hall, CB#3280

Phone : (919) 962-6932
Fax: (919) 962-1625
E-mail: alan_jones@unc.edu

The author responsible for distribution of materials integral to the findings presented in this article is Dr. Alan Jones alan_jones@unc.edu

Running Title: Biased System Signaling

Title: Biased Signaling: Distinct Ligand-directed Plasma Membrane Signalosomes Using a Common RGS/ G protein Core

AUTHORS Timothy J. Ross-Elliott[1], Justin Watkins[1], Xiaoyi Shan[2], Fei Lou[1], Bernd Dreyer[1], Meral Tunc-Ozdemir[1], Haiyan Jia[1], Jing Yang[1], Luguang Wu[2], Yuri Trusov[3], Patrick Krysan[4], and Alan M. Jones[1, 3, 5]

Department of [1] Biology and [3] Pharmacology, University of North Carolina at Chapel Hill, Chapel Hill, NC 27599, USA.

[2]Beijing Forestry University, Beijing China 1000083

[3]School of Agriculture and Food Science, The University of Queensland, St. Lucia, Q4072, Australia.

[4]Department of Horticulture, University of Wisconsin Madison, Madison, WI 53706, USA

[5]Lead Contact

*Correspondence: alan_jones@unc.edu

Keywords: Arrestin analog, AtRGS1, calcium signaling, clathrin-mediated endocytosis, MAPK activation, proximity labeling, sterol-dependent endocytosis, VPS26, WNK kinase,

Abbreviations: *Arabidopsis thaliana* Regulator of G Signaling (AtRGS1), Clathrin-Mediated Endocytosis (CME), Sterol-Dependent Endocytosis (SDE), Total Internal Reflection Fluorescence Microscopy (TIRF), Clathrin Light Chain (CLC), Flotilin 1 (FLOT1), Vacuolar Protein Sorting 26 (VPS26)

SUMMARY

Biased signaling occurs when different ligands that are directed at the same receptor launch different cellular outcomes. Because of their pharmacological importance, we know the most about biased ligands and little is known about other mechanisms to achieve signaling bias. In the canonical animal G protein system, endocytosis of a 7-transmembrane GPCR desensitizes a cell from its extracellular signal. β-arrestins facilitate GPCR endocytosis but also propagate cytoplasmic signaling depending on the bias. In Arabidopsis, GPCRs are not required for G protein coupled signaling because the heterotrimeric G protein complex spontaneously exchanges nucleotide. Instead, the prototype 7-transmembrane Regulator of G Signaling 1 protein AtRGS1 modulates G signaling and through ligand-dependent endocytosis, de-repression of signaling is initiated but canonical arrestins are not involved. Endocytosis initiates from two separate pools of plasma membrane: microdomains and a clathrin-accessible neighborhood, each with a select set of discriminators, activators, and newly-discovered arrestin-like adaptors. Different trafficking origins and trajectories lead to different cellular outcomes. Thus, compartmentation with its attendant signalosome architecture is a previously unknown mechanism to drive biased signaling.

INTRODUCTION

Different ligands discriminated by the same receptor or utilizing the same core of signaling elements can set in motion a cascade of events that lead to multiple outcomes. When subsets of outcomes are ligand-specific, we label this biased signaling. This bias can be encoded in the ligand structure (biased ligands), in the receptors (biased receptors), or in the interactions between the signaling components (biased systems) (Smith et al., 2018). Of the three defined mechanisms,

biased ligands is the most widely studied because of its immediate pharmacological significance, such as the development of drugs that provide analgesia without the addictive side effect (Manglik et al., 2016; White et al., 2015; Wingler et al., 2019). **a)** Ligand bias occurs when a ligand stabilizes one or few of several conformations of a receptor protein which then preferentially recruits or activates signaling elements such as arrestin and the heterotrimeric G protein complex that lead toward one cellular outcome over another (Bohn et al., 2000; DeWire et al., 2013). For example, some ligands are biased towards β-arrestins (aka arrestin-2 and -3) signaling (Charest et al., 2007; Gesty-Palmer et al., 2006; Shenoy et al., 2006) such as certain dopamine agonists compared to dopamine which is biased towards D_2R-β-arrestin coupling (Allen et al., 2011). Certain opioid agonists compared to morphine are biased toward G-protein signaling (DeWire et al., 2013; Rives et al., 2012; White et al., 2015). **b)** Receptor bias occurs through recognition of the same ligand by multiple receptor types (Géhin et al., 1999) including so-called decoy receptors (Lin and Hsieh, 2011; Pan et al., 1997), some of which may in fact be functional receptors that use non-classical signaling pathways (Lin and Hsieh, 2011; Rajagopal et al., 2010a). Dopamine D_1 and D_2 class receptors recognize dopamine, but signal through different subunits of Gα as well as arrestin (Urs et al., 2017). **c)** System bias involves a cell-mediated shift to one pathway over another by some unknown mechanism but one possibility is through mass action, for example, making arrestin more abundant at the receptor than Gα or a particular kinase (Urs et al., 2016). This last category of bias signaling is the least understood and the subject of the present work.

Phosphorylation patterns are the chemical bar codes for biased signaling at least for arrestin-dependent outcomes (Butcher et al., 2011; Nobles et al., 2011; Shiraishi et al., 2018; Yang et al., 2015; Yang et al., 2017). G-protein coupled Receptor Kinases (GRKs) phosphorylate the C-terminus or other cytoplasmic elements of GPCRs in response to agonist binding (Choi et al.,

2018), unlike Protein Kinase A and C that phosphorylate GPCRs in a heterologous manner (Benovic et al., 1986; Sibley et al., 1987). The subsequent coupling of arrestin to phosphorylated GPCRs does not end G-protein-independent signaling. Arrestin-bound GPCRs further activates some multiple kinase pathways including MAPK and tyrosine kinases (DeFea et al., 2000; Luttrell et al., 2001; Rajagopal et al., 2010b) but not all (e.g. (O'Hayre et al., 2017)). While plants lack GRKs, an Arabidopsis family of kinases called WITH NO LYSINE (**WNK**) Kinase phosphorylate the C-terminal tail of the non-canonical 7-transmembrane Regulator of G Signaling (**AtRGS1**) in response to extracellular glucose (Fu et al., 2014; Urano et al., 2012). AtRGS1 is also phosphorylated by other kinases including BAK1, a co-receptor for flg22 which is a Pathogen-Associated Molecular Pattern (PAMP) (Liang et al., 2018; Tunc-Ozdemir et al., 2017; Tunc-Ozdemir et al., 2016) and loss of AtRGS1 and other G protein components severely affect resistance in a wide range of pathogens (Zhong et al., 2018). System-biased signaling may be particularly relevant in plants where AtRGS1 modulates intracellular signaling transduction through G protein activation. AtRGS1 regulates G protein activation with ligand discrimination likely facilitated by membrane bound Receptor Like Kinases (RLKs) of which there are more than 600 members in Arabidopsis (Shiu and Bleecker, 2001).

In animals, activation of G Protein signaling results from GDP exchange for GTP on the Gα subunit, wherein this nucleotide exchange is the rate-limiting step (Ferguson et al., 1986). Desensitization of the cell toward the signal occurs through endocytosis of the GPCR mediated by arrestins (Benovic et al., 1987; Lohse et al., 1990). In Arabidopsis, however, the Gα subunit, AtGPA1, spontaneously exchanges nucleotides without a GPCR thus it is self-activating with the intrinsic GTPase activity being the rate-limiting step (Johnston et al., 2007; Jones et al., 2011a). AtRGS1 accelerates the intrinsic GTPase of AtGPA1 (Jones et al., 2011b) and as a result, inactive

Gα remains bound to GDP until de-repression through AtRGS1 endocytosis, permitting Gα activation through nucleotide exchange and subsequent downstream signal transduction (Urano et al., 2012). This AtRGS1 endocytosis is a well-established proxy for sustained G protein activation and the proportion of endocytosed AtRGS1 is linearly related to the proportion of G protein activation (Fu et al., 2014). In Arabidopsis, sugars (Fu et al., 2014; Grigston et al., 2008) and flg22 (Tunc-Ozdemir et al., 2016) activate AtRGS1 (Urano et al., 2012).

Physically de-coupling AtRGS1 from the heterotrimeric G protein complex by endocytosis is the engine of the de-repression mechanism, at least for sustained activation. There are two modes of endocytosis in plants: Clathrin-Mediated Endocytosis (**CME**) and Sterol-Dependent Endocytosis (**SDE**) (Fan et al., 2015), however, the protein that directly couples to AtRGS1 and is responsible for endocytosis is unknown. Extensive work elucidated the CME pathway in animal and yeast systems with the function of many molecular components being well characterized. Of particular interest is the ADAPTOR PROTEIN COMPLEX-2 (**AP-2**) that is required for recognition and binding of cargo (Jackson et al., 2010; Kelly et al., 2008; Krauss et al., 2006), recruiting clathrin to the PM, and the subsequent formation of clathrin-coated vesicles. In the absence of AP-2 function, clathrin-coated vesicle formation is reduced and endocytosis is inhibited (Boucrot et al., 2010). The AP-2 complex is a heteromeric complex consisting of 2 large subunits (α2 and β2), 1 medium subunit (μ2), and 1 small subunit (σ2) (Collins et al., 2002).

SDE is a clathrin-independent mechanism for internalization of membrane-associated proteins. Sometimes referred to as lipid raft endocytosis, SDE of these microdomains requires flotilin1 (**Flot1**), and possibly the microdomain-associated remorin protein (Raffaele et al., 2009) for internalization of sterol-rich vesicles (Li et al., 2012). Membrane proteins PIP2;1 and

Respiratory Burst Oxidase Homolog D (**RbohD**) are selectively internalized via sterol-dependent endocytosis under salt stress conditions (Hao et al., 2014; Li et al., 2011).

We present data illustrating a biased system where two distinct extracellular ligands induce endocytosis of AtRGS1 from separate plasma membrane origins, of which one is mediated by a an arrestin-fold-containing protein, Vacuolar Protein Sorting 26 (VPS26). flg22 initiates AtRGS1 endocytosis via CME, while glucose activates both pathways of endocytosis. Phosphorylation of AtRGS1 and involvement of individual subunits of the heterotrimeric G protein complex are also ligand specific as are the immediate downstream consequences. From the CME-mediated-AtRGS1 origin, flg22 induces a MAPK cascade known to drive transcriptional reprogramming (Lee et al., 2015), whereas from the SDE-mediated-AtRGS1 origin, glucose induces transcriptional change that is independent of the MAPK cascade.

RESULTS

Biased Signaling by Two Extracellular Signals

To date, there are 2 well-studied signals that directly and rapidly activate the Arabidopsis heterotrimeric G protein signaling pathway through AtRGS1 endocytosis: **1)** flg22 which is a 22-amino acid PAMP from the plant pathogen *Pseudomonas syringe* that is recognized on plant cells to initiate the innate immunity pathway (Asai et al., 2002; Felix et al., 1999; Gómez-Gómez and Boller, 2000). It is already established that flg22 is perceived extracellularly (e.g. (Jelenska et al., 2017) by co-receptors BAK1 and FLS2 as part of a larger G protein complex (Sun et al., 2013; Tunc-Ozdemir and Jones, 2017). **2)**. Glucose or a glucose metabolite which are products of photosynthesis (Tunc-Ozdemir et al., 2018) and metabolism of starch stores (Pharr and Keller, 2017).

Many sugars, although primarily sucrose, are transported extracellularly in the apoplastic space where they are converted to glucose by cell wall localized invertases and potentially further metabolized to a signal. These sugars are rapidly taken up through a large family of transporters (Chen et al., 2010; Williams et al., 2000) where they are detected in the cytoplasm, but some sugars may also be detected extracellularly (Li and Sheen, 2016). D-glucose or its metabolite induces rapid endocytosis of AtRGS1-dependent sugar signaling (Fu et al., 2014; Urano et al., 2012) and because AtRGS1 shares the membrane topology of GPCRs which perceive extracellular signals, it has been assumed that the extracellular glucose or metabolite is perceived by the AtRGS1/G protein complex. However, neither an extracellular site for perception nor direct evidence for agonist binding to AtRGS1 has been shown. To address the former, impermeant sugars were tested for the ability to activate G signaling.

The glucose-fructose dissacharide 6-0-α-D-glucopyranosyl-D-fructose (aka isomaltulose, pallatinose), is presumed not to be transported across the plant cell membrane although it acts as an active glucose precursor if synthesized intracellularly (Loreti et al., 2000; Sinha et al., 2002). While the expression of sucrose isomerase in potato increased apoplastic isomaltulose, transport across any membrane has yet to be demonstrated (Börnke et al., 2002). Importantly, isomaltulose is not hydrolyzed extracellularly (Fernie et al., 2001; Wu and Birch, 2011). To determine if isomaltulose is impermeant to the plasma membrane, we chemically synthesized [^{14}C] isomaltulose (Figure S1A) and tested for uptake into Arabidopsis seedlings. Isomaltulose was at least 9-fold less permeant to cells than glucose (Figure S1B). Therefore, to determine if sugars are perceived extracellularly by hypocotyl cells, we tested the effect of isomaltulose on AtRGS1-YFP endocytosis (Figure 1A) as a validated proxy for activation of G signaling as previously shown (Fu et al., 2014; Urano et al., 2012). Whereas several mono and disaccharides failed to activate G

signaling, extracellular isomaltulose caused AtRGS1 internalization more effectively ($P < 0.01$) than D-glucose (Figure 1B) despite being transported ~10-fold less suggesting that isomaltulose activates AtRGS1 extracellularly. The 5% D-glucose impurity in the isomaltulose preparation would induce at most 5% AtRGS1 internalization and therefore does not account for the observed level of activation. Turanose is another disaccharide that is thought to be perceived extracellularly (Loreti et al., 2000) and is impermeant (Rolland et al., 2002) therefore endpoint analysis was performed using this sugar, and just as for both glucose and isomaltulose, turanose activated G signaling (Figure 1C). Isomaltulose and turanose are disaccharides that share a glucose ring (Figure 1D), suggesting that glucose or a glucose metabolite is the discriminated signal or is important for a metabolic agonist (e.g. sugar nucleotides).

AtRGS1 Endocytic Pathway is Signal Biased

Having shown that extracellular flg22 is detected by BAK1/FLS2 (Chinchilla et al., 2006; Gómez-Gómez and Boller, 2000; Tunc-Ozdemir et al., 2016) and induces AtRGS1 endocytosis (Tunc-Ozdemir et al., 2016) and that extracellular D-glucose acts upstream of AtRGS1 endocytosis, both requiring at least in part the phosphorylation of AtRGS1 at its C terminal tail (Tunc-Ozdemir et al., 2016; Urano et al., 2012), we turned to the question of whether these two signals activate the same pool of AtRGS1. Endocytosis in plants utilizes two primary pathways: CME and SDE. Both pathways have been individually associated with the activity of specific proteins and responses (Adam et al., 2012; Dhonukshe et al., 2007; Irani et al., 2012; Li et al., 2012); for example, CME and SDE cooperatively regulate the activity of RbohD in the flg22 pathway (Hao et al., 2014). We used high-resolution microscopies to achieve the needed spatial and temporal resolution to answer quantitative differences in signal-induced activation. To determine if one or both pathways regulate AtRGS1 activity at the membrane, we induced internalization with D-glucose and *flg22*

while simultaneously inhibiting the CME pathway by arresting AP2µ function with TyrphostinA23 (**TyrA23**) (Banbury et al., 2003; Dhonukshe et al., 2007) or inhibiting the SDE pathway by suppressing microdomain formation via sterol solubilization with methyl-β-cyclodextrin (**MβCD**) (Ilangumaran and Hoessli, 1998; Ohtani et al., 1989). MβCD, even at great excess, did not block *flg22*–induced AtRGS1 internalization compared to the control ($p<0.01$) (Figure 2A). Conversely, AtRGS1 internalization induced with glucose was reduced nearly 50% compared to baseline with a minimum concentration of 5mM MβCD (Figure 2B). This suggests that roughly half of the D-glucose-regulated pool of AtRGS1 is located in a SDE domain. To determine if the CME pathway regulates AtRGS1 activity, we applied TyrA23 with *flg22* or D-glucose. AtRGS1 internalization with both activators was significantly reduced ($p<0.01$); completely for flg22-induced AtRGS1 endocytosis (Figure 2C) and by 50% for D-glucose-induced AtRGS1 endocytosis (Figure 2D). The structurally similar but inactive TyrA23 analog TyrphostinA51 showed no significant effect on AtRGS1 internalization ($p<0.01$) (Figure 2C and 2D, TyrA51), indicating that the inhibitory effect of TyrA23 is chemically specific (Banbury et al., 2003). When both inhibitors were applied simultaneously with glucose, AtRGS1 internalization was ablated (Figure 2E). These results suggest that there is a single flg22-induced pool that internalizes through a CME pathway and that there are two distinct glucose-induced pools, one internalizes through the CME pathway and the other through the SDE pathway. Because the glucose-induced pool is equally inhibited by the CME and SDE inhibitors, a rapid equilibrium between the pools is not likely, otherwise neither inhibitor would have shown efficacy.

To further test our hypothesis of ligand-dependent membrane origins of AtRGS1 endocytosis, we used a genetic approach by measuring AtRGS1 internalization in the AP-2µ null mutant, *ap2m* (Kim et al., 2013). The AP-2 complex plays a critical role in transporting cargo in

the CME pathway, whereby the μ subunit of this tetrameric AP-2 complex directly interacts with cargo proteins during endocytosis (Bashline et al., 2013; Krauss et al., 2006). In the *ap2m* mutant seedlings, flg22-induced AtRGS1 internalization was ablated ($p<0.01$), consistent with the TyrA23 results (Figure 2F). In contrast, glucose resulted in less AtRGS1 internalization in the *ap2m* mutant compared to Col-0 wild type ($p<0.01$). The addition of MβCD with glucose ablated AtRGS1 internalization in the *ap2m* mutant to basal levels (Figure 2G). These observations are consistent with two signal-dependent pools of AtRGS1 on the plasma membrane; 1) a homogenous pool for flg22 signaling and 2) a conglomerate pool for D-glucose signaling.

A Point Mutation in the 7 Transmembrane Domain Disarms Biased Signaling

The μ subunit of the AP-2 complex is a cargo recognition and interaction component in the CME pathway. It binds to known tyrosine motifs, YXXΦ, where X is any amino acid and Φ is an amino acid with a hydrophobic side chain (Ohno et al., 1995). The second cytoplasmic loop in AtRGS1 contains such a motif with the amino acid sequence Y^{112}FIF (Chen et al., 2003). To determine if this motif is necessary for AtRGS1 endocytosis and a potential binding motif for AP-2μ, we generated AtRGS1 with a tyrosine to alanine mutation (AtRGS1^{Y112A}). flg22 failed to induce endocytosis of the AtRGS1^{Y112A} mutant (Figure 2H). Glucose-induced internalization of the AtRGS1^{Y112A} was reduced to half ($p<0.05$) compared to wild type internalization and was further reduced to the resting level with the addition of MβCD ($p<0.01$) (Figure 2I) demonstrating that the Y^{112}FIF is necessary for internalization and likely a recognition and binding site for AP-2μ. The flg22-induced AtRGS1 pool is entirely mediated by the CME pathway whereas roughly half of the D-glucose-induced AtRGS1 pool internalizes through the CME pathway.

Physically-Distinct, Dynamic Populations of AtRGS1: Architectural Basis for Biased Signaling

We showed through pharmacological and genetics approaches that two signal-dependent pools of AtRGS1 exist raising the possibility that the two AtRGS1 pools are physically distinct on the cell membrane. The differential dependence on sterol and clathrin for partial glucose- vs. flg22-induced endocytosis of AtRGS1 suggests this is the case. To test this hypothesis, we imaged AtRGS1 with a GFP C-terminal tag using Total Internal Reflection Microscopy (**TIRF**) and IMARIS (v9.2.2, Bitplane Inc) surface tracking (Figure S2 A-E, examples of raw data). We calculated the average size and speed of AtRGS1 proteins during a 30-second interval taken from time-lapse imaging at 5 and at 15 minutes post treatment with glucose and flg22. Two clearly distinct signal-dependent populations of AtRGS1 were observed (Figure 2J). After 5 minutes under glucose conditions, the surface area of AtRGS1-GFP clusters were significantly larger ($\ddot{x}$ = 0.9403 μm^2 n=4619) than flg22 at ($\ddot{x}$ = 0.5998 μm^2 n=2026) (Figure 2J inset) ($p<0.01$). At 15 minutes, the area of flg22 treated AtRGS1-GFP increased slightly to 0.6733 μm^2 (n=1751), with glucose treated AtRGS1-GFP, the area increased to 1.0072 μm^2 (n=6209) (Figure S2 F-H). Velocity differences for AtRGS1-GFP remain consistent between 5 and 15 minutes with flg22-treated AtRGS1 averages at 1.53µm/s and 1.63µm/s, respectively (n= 2026 and 1751) and glucose-treated AtRGS1 averages at 0.98µm/s and 1.01µm/s at 5 and 15 minutes, respectively (n= 4619 and 6209). Two populations of differently sized AtRGS1 protein clusters provides structural support for two origins of endocytosis.

The Signal Dependency Correlates with Endocytosis Marker Redistribution

The Clathrin Light Chain (**CLC**) and Flot1 proteins are associated with CME and SDE, respectively (Fan et al., 2015; Li et al., 2012). We generated transgenic lines expressing AtRGS1-

GFP with either CLC-mCherry or Flot1-mCherry endocytosis markers to investigate the localization of AtRGS1 in relation to both markers. We imaged the response of both endocytosis markers 5 minutes after application of water, flg22, and glucose to look for changes in marker distribution in the cell (Figure 2K-P). Using Manders Overlap Coefficient, we quantified the co-occurrence of both endocytosis markers with AtRGS1-GFP under all treatment conditions. We are using Manders instead of Pearson's Correlation because our qualitative analysis shows a ligand dependent change in marker localization and shape. We simply want to quantify the change in overlap of the two signals (Manders) and not the change in signal intensity (Pearsons) that may simply be a result of AtRGS1 internalization and not correlated to direct interaction with either endocytosis marker.

A subset of the Manders Overlap Coefficients after background subtraction are shown in Figure 2Q-V and correspond to the confocal micrographs in Figure 2K-P. M1 represents the proportion of total GFP that overlaps with mCherry. Similarly, M2 represents the proportion of total mCherry for CLC or FLOT1 that overlaps with GFP. Under conditions with no signaling ligand (Figure 2K and 2N), RGS1-GFP and our endocytosis markers have a high overlap baseline (Figure 2Q and 2R). Due to the restrictive cytoplasmic space, we believe this is not functional interaction, merely fluorescence overlap due to high protein crowding and resolution limitation. After flg22 addition (Figure 2L and 2O), the proportion of CLC associated with RGS1 decreased, with the proportion of RGS1 overlapping with CLC also decreasing significantly ($p<0.01$) (Figure 2S. Simply stated, a smaller defined subset of the RGS1 and CLC populations are overlapping with each other in a ligand-dependent manner with the endocytosis marker also exhibiting a structural change. This response was not observed with FLOT1 when flg22 was added (Figure 2T). With glucose addition (Figure 2M and 2P) CLC showed no significant change compared to

297 water (Figure 2U), while FLOT1 overlap decreased with RGS1 compared to the water baseline
298 ($p<0.01$) (Figure 2V). The same responses were observed at 15 minutes post ligand addition
299 (Figure S2 I-T). The averages for the entire collection of M2 scores from all samples are presented
300 in Figure 2W. These results indicate that endocytosis markers are responding to specific ligands
301 and subsets of the total marker and AtRGS1 protein populations are overlapping in a signal specific
302 manner. In summary, the different intrinsic trafficking properties further support at least two pools
303 of ligand-activated AtRGS1.

304 **Signaling Bias Involves Phosphorylation from Different Kinases.**

305 Phosphorylation of AtRGS1 is a necessary requisite for both glucose- and flg22-induced
306 endocytosis. The C-terminus of AtRGS1 contains multiple di-serine residues that could function
307 as potential phosphorylation sites for signal transduction. A truncated version of AtRGS1 lacking
308 the 43 most C-terminal residues, AtRGS1$^{\Delta Ct}$, served as a blunt phosphorylation-deficient mutation
309 to determine if the C-terminal tail, in particular any C-terminal serines located there are necessary
310 for AtRGS1 endocytosis (Figure S4A). Application of flg22 failed to internalize the AtRGS1$^{\Delta Ct}$
311 mutant compared to water control ($p<0.01$) (Figure 3A). Glucose application however, internalized
312 the AtRGS1$^{\Delta Ct}$ mutant, but at 50% the level of the wild type AtRGS1 ($p<0.01$). MβCD completely
313 inhibited internalization of the AtRGS1$^{\Delta Ct}$ mutant levels ($p<0.01$) (Figure 3B). These results show
314 that the C-terminus is necessary for flg22- and glucose-induced endocytosis of AtRGS1 and
315 support two subpopulations of AtRGS1 among the glucose-induced pool.

316 Three phosphorylated serine residues on the C-terminus of AtRGS1 at positions 428, 435,
317 and 436 are necessary for at least partial endocytosis of AtRGS1 induced by both glucose and
318 flg22. Therefore, we mutated these serines to alanine (AtRGS1^{3SA}) to determine if those specific
319 residues were necessary to induce internalization by either agonist. Upon treatment with flg22,

AtRGS1^{3SA} internalization was at basal levels compared to wild type ($p<0.01$) (Figure 3C), confirming previous results by Tunc-Ozdemir *et al* (Tunc-Ozdemir et al., 2016) and suggesting that the CME pathway is dependent on phosphorylation of serines 428, 435 and/or 436. In the case of glucose, endocytosis was only partially impaired by the AtRGS1^{3SA} mutant ($p<0.01$) (Figure 3D). MβCD completely blocked glucose-induced endocytosis of the AtRGS1^{3SA} mutant (Figure 3D), consistent with our previous results that show glucose-induced internalization utilizes both CME and SDE pathways and that the CME pathway requires phosphorylation at Ser$_{428/435/436}$.

These results enable us to exclude an osmotic effect that effectively sequesters a portion of the plasma membrane pool of AtRGS1 into a sterol-dependent, or at least an MβCD-inhibitable, microdomain that is incapable of internalizing its components. If an osmotic effect occurred, the presence of MβCD would have prevented formation of these microdomains and consequently the sequestration of AtRGS1 for the endocytic pool would cause 100% internalization by glucose. This was not observed.

System Bias by Skewed Kinase and G-protein Complex Composition

Because the cluster of phosphorylated serines on the C-terminus of AtRGS1 are required for AtRGS1 internalization, we hypothesize that one mechanism for system bias is to functionally-sequester cognate kinases for glucose and flg22 in their respective ligand-delineated pools. To test this hypothesis, we quantified AtRGS1 internalization in the mutant backgrounds of the flg22-activated FLS2 kinase (*fls2*) and BAK1 co-receptor (*bak1*) and the D-glucose-activated WNK kinase (*wnk8*-2, *wnk1*-1) null mutants. Upon treatment with flg22, AtRGS1 endocytosis was ablated in *fls2* and *bak1-4* mutants ($P<0.01$), while glucose-induced internalization in these mutants was unaffected ($P=0.70$ and 0.37 respectively) (Figure 3E and 3F). In contrast, D-glucose-induced internalization in the *wnk8-2* was ablated ($p<0.01$), while flg22-induced AtRGS1

343 endocytosis was unaffected (P=0.89) (Figure 3G). Interestingly, a low dose, long duration
344 application of 2% glucose over 6 hours to *wnk1-1* had no discernable affect compared to wild type
345 (Figure S3A), prompting a revisit of the proposed mechanism that WNK1 kinase mediates low
346 dose-long duration activation by glucose (Fu et al., 2014). Our results suggest that FLS2 and
347 BAK1 are specific to the CME pathway and WNK8 kinase is specific to the SDE pathway.
348 The canonical components of the heterotrimeric G protein complex are necessary for
349 glucose-induced internalization of AtRGS1 (Fu et al., 2014; Urano et al., 2012). More specifically,
350 Gβγ is required for the recruitment of WNK kinases for phosphorylation of AtRGS1, leading to
351 AtRGS1 endocytosis and activation of downstream G signaling. We hypothesized that individual
352 components of the G protein heterotimer may be required for biased signaling. To test this
353 hypothesis, we quantified AtRGS1 endocytosis in G protein mutant backgrounds after flg22 and
354 glucose activation. In the AtGPA1 (Gα) null background, *gpa1-4,* AtRGS1 endocytosis showed
355 no significant difference compared to wild type when glucose was applied (p=0.48) (Figure 3H).
356 After addition of flg22, however, AtRGS1 endocytosis was at basal levels ($p < 0.01$) in the absence
357 of Gα indicating that the G subunit is essential for this pathway (Figure 3H). We additionally tested
358 AtRGS1 in the absence of XLG2, one member of a three-gene family of atypical, G proteins. XLG
359 proteins have a homologous C-terminal Gα domain and N-terminal nuclear localization signal
360 (Ding et al., 2008). Loss of XLG2 in the *xlg2-1* mutant, did not affect AtRGS1 endocytosis by
361 glucose application (p=0.43), but completely inhibited AtRGS1 endocytosis to basal levels after
362 addition of flg22 ($p<0.01$) (Figure 3I). Additionally, low dose, long duration glucose application
363 had no effect in the *xlg2*-1 mutant compared to wild type (Figure S3B). In the *agb1-2/agg1* double
364 null mutant, AtRGS1 endocytosis was diminished after addition of flg22 ($p<0.01$) (Figure 3J).
365 Loss of the Gβγ dimer in the *agb1-2/agg1* mutant had no effect on glucose-induced AtRGS1

endocytosis compared to wild type after 30 minutes of treatment with 6% D-glucose ($p=0.79$) (Figure 3J). Interestingly, a 2% - 6 hour application of D-glucose required AGB1/AGG1 for activation ($p<0.01$) (Figure 3K).

VPS26 a Candidate Plant β-arrestin-like Adaptor Necessary for AtRGS1 Endocytosis in the CME Pathway: Discovery and Validation

In the animal G signaling pathway, GPCR endocytosis results in β–arrestin-mediated desensitization of the cell from an extracellular signal. Higher plant genomes do not encode ancestral α-arrestins or canonical (i.e. visual and nonvisual) arrestins (Alvarez, 2008). We sought candidate adaptors for AtRGS1 that may function like β-arrestins to recruit AP2/clathrin to AtRGS1 for endocytosis by querying 3-D structure databases. As shown in Figure S4A and B, we identified three *Arabidopsis* VACUOLAR PROTEIN SORTING 26 (VPS26) proteins that contain arrestin folds (Oliviusson et al., 2006) and are orthologous to human VPS26. *Arabidopsis* VPS26A and VPS26B amino acid sequences are 91% identical whereas VPS26-like is 20% identical to VPS26A and VPS26B. In mammals and plants, VPS26 operates with VPS29 and VPS35 in the retromer complex on the endosome (Zelazny et al., 2013). This raises the possibility that VPS26 proteins have a moonlighting function in modulating AtRGS1 internalization.

To compare the arrestin and AtVPS26A protein structures, we first created a model of AtVPS26A using MODELLER (Martí-Renom et al., 2000). Toward this, a high quality homogeneous sequence alignment was generated using the VPS26 family (Arabidopsis VPS26A, VPS26B, VPS26like and Homo sapiens VPS26A) and arrestin family (Vertebrates: Human arrestin-1 and arrestin-2; bovine arrestin-1, arrestin-2, arrestin-2, and a variant p44; Squid arrestin-1; and the invertebrate shrimp arrestin (Figure S5A). Human, bovine, and squid sequences were included because PDB structures are available. The squid and shrimp sequences were added for

divergence information (among the opistokonts). AtVPS26A and human VPS26A share 56.48% sequence identity while AtVPS26A and arrestins share only 14-17% sequence identities (Figure S5B). These results rationalized our use of the high-resolution (2.1Å) crystal structure of *Homo sapiens* Vps26a (PDB [2FAU]) rather than an arrestin structure to generate models of AtVPS26A for subsequent comparison to arrestin. Details of the top five selected models (atvps26a1 →5) are provided in the Methods.

We compared the atvps26a-2 model with the bovine arrestin-3 (PDB [3P2D (Zhan et al., 2011)]). Although the primary amino acid identity between arrestin and AtVPS26A is only ~15% (Figure 4A), the structure of AtVPS26A model shows a remarkably similar arrestin scaffold with arrestin which contains a semi-symmetric fold of two β strand sandwich structures in the N domain and C domains linked by the central loops with each sandwich formed by 3 or 4 β sheets, respectively.

For arrestin, the conserved structures mainly include the N-terminal and C-terminal arm, central crest comprised of a finger loop (Hirsch et al., 1999), a middle loop (Kim et al., 2012; Shukla et al., 2013); see box ii of Fig. 4) and C loop (Kang et al., 2015) see box I of Fig. 4), Figure 4A), the gate loop, polar core, and the hinge domain (Peterson and Luttrell, 2017). The N-terminal and C-terminal arms stabilize the arrestin conformation. Model atvps26a-2 shares similar N-terminal and C-terminal scaffolds with arrestin however it lacks a short α-helix inside the arrestin N-terminal domain (Figure 4B) which has been implicated in receptor binding (Vishnivetskiy et al., 2011). In addition, arrestin has a longer C-terminal tail, which extend all the way to bind the N terminal domain, important for linkage to enable CME. The C terminus of atvps26a-2 has no extension however some arrestins also have a short C-tail (Gurevich and Gurevich, 2006).

411 The overall central crest of atvps26a-2 is similar with that of arrestin which includes the
412 finger loop, middle loop and the C loop (Figure 4C). While arrestin has a longer finger loop
413 important for receptor binding. The rearrangement of the finger loop is a major change associated
414 with arrestin activity, likely serving as a critical part of the activation sensor (Chen et al., 2018).

415 The polar core is the key component of the phosphate sensor. In arrestin, the polar core is
416 comprised of five charged side chains including two Arg and three Asp that are essential to its
417 activation (Vishnivetskiy et al., 1999). The residues in the polar core of bovine arrestin-3 are:
418 Asp_{27}, Arg_{170}, Asp_{291}, Asp_{298} and Arg_{393} (Figure 4D and E). The human vps26A also contains a
419 polar core between the N terminal and C terminal domains which includes the N domain residues
420 Glu_{119} and Tyr_{121}, and C domain residues Lys_{213}, Glu_{215}, Thr_{258}, Tyr_{272}, and Arg_{296} (Shi et al.,
421 2006). The residues of the polar core of VPS26 are conserved suggesting that they play a critical
422 role in protein function. We thus labeled the polar core of atvps26a according to the human vps26a
423 template. The residues of atvps26a are the N-domain residues Glu_{118} and Tyr_{120}, and C domain
424 residues Arg_{213}, Glu_{215}, Thr_{258}, Tyr_{272}, and Arg_{296} (Figure 4 F and G). Although different amino
425 acid composition, both cores consist of positive charged residues and allow the formation of
426 hydrogen bonds under physiological conditions. However, the orientation and shape of the polar
427 core of VPS26 is distinct from arrestin. The arrestin polar core is embedded between β sheets in
428 the N terminal domain whereas the VPS26 core is open and elongated, spanning the length of
429 space between the N domain and C domain.

430 The most divergent arrestin structure from 3P2D is a 3Å-resolved truncated arrestin from
431 squid (PDB 1CF1, (Bandyopadhyay et al., 2018). Unlike for bovine arrestin, the C-tail interaction
432 with the gate loop of the polar core is weak and flexible. This functional divergence between

433 squid and human arrestin, both recruited to receptors, tempers the impact of the lack of a long C-
434 tail in the atvps26a-2 model.

435 Taken together, these similarities between AtVPS26 and arrestin prompted the hypothesis
436 that AtVPS26 is a candidate adaptor for CME of AtRGS1. Therefore, we isolated null alleles of
437 the three VPS26 genes in Arabidopsis: VPS26A, VPS26B, and VPS26-LIKE (aka VPS26C) (Jha
438 et al., 2018; Zelazny et al., 2013) and phenotyped the hypocoty length at 5 days, the relevant stage
439 for our cytological analyses. As shown in Figure S4F, there were no qualitative differences
440 between VPS26 null mutants and Col-0 precluding any developmental basis for alterations in
441 AtRGS1 activation in these mutants. In addition, the AtRGS1-YFP reporter was combined with
442 the mutant backgrounds through generating stable transformants. As shown in Figure 4H, loss of
443 either VPS26A or VPS26B dramatically reduced the flg22-induced internalization of AtRGS1 to
444 levels that are not statistically different from the baseline level ($p=0.34$) whereas loss of VPS26-
445 like had no statistical effect on AtRGS1 internalization by flg22 ($p=0.65$). Loss of any of the three
446 VPS26 proteins had no statistical effect on glucose-induced internalization of AtRGS1 ($p<0.001$)
447 suggesting that VPS26A/B are involved in flg22- but not glucose-induced AtRGS1 endocytosis.
448 To confirm that VPS26 is not involved in glucose-induced AtRGS1 internalization, we quantitated
449 the CME and SDE portions of this trafficking pathway in the *vps26* mutants. As shown in Figure
450 4I, in each of the *vps26* mutant backgrounds, both the TyrA23A and MβCD-inhibitable segments
451 of the glucose-induced internalization of AtRGS1 remained intact. This suggests that the TyrA23-
452 dileneated (CME) pathway used by AtRGS1 when activated by flg22 differs from the TyrA23A-
453 dileneated pathway activated by D-glucose.

454 The genetic data suggest that VPS26A and B form dimers. To test if VPS26 A and B
455 subunits heterodimerize *in vivo*, BiFC analysis was conducted and showed that heterodimers can

form from ectopically-expressed monomers and suggested that the orientation is head-to-tail (Figure 5A). Self-association of arrestin family members also occurs and may be part of a regulatory mechanism for arrestin activation (Chen et al., 2014). For relative quantitation of *in vivo* interaction, split luciferase was performed and found that the strongest interaction was between VPS26A and VPS26B (Figure 5B). VPS26B dimers form under these conditions but not VPS26A dimers or any oligomer with VPS26Like subunits. We have yet to find conditions which allow stable expression of VPS26 subunits tagged with a full-length auto-fluorescent protein in Arabidopsis suggesting that the additional mass of the tag prevents dimer formation and that monomers are unstable.

To test if the full-length AtRGS1 protein interacts with the VPS26 subunits *in vivo*, BiFC, split luciferase, and Y2H analyses were performed. Fluorescent complementation of YFP by AtRGS1-nYFP with cYFP-VPS26A and with VPS26B-cYFP was observed (Figure 5C). The split luciferase assay confirmed that this interaction is as strong as the interaction between AtGPA1 and its AGB1/AGG1 partner (Figure 5D). Finally, Y2H showed that the interaction between AtRGS1 and VPS26 is direct. The entire C-terminal half of AtRGS1 (thus lacking the 7 TM domain) interacts with VPS26B. Surprisingly, removal of the post RGS-box C-terminal tail which includes the $Ser_{428,435,436}$ phosphorylation cluster did not ablate this interaction however, additional loss of two other phosphorylated Ser located between helices VII and VIII of the RGS box completely abolished the interaction.

Biased Signaling Outputs

While both D-glucose and flg22 result in different RGS1-YFP trafficking, we asked what other signaling outputs distinguish these ligands. Two rapid events of the flg22 response is the induction

of MITOGEN ACTIVATED PROTEIN KINASE 6 (MPK6) activity and Ca^{2+} signaling (Ranf et al., 2011). To test the impact of flg22 and D-glucose on MPK6 activity in etiolated hypocotyls, we developed a FRET-based sensor that measures kinase activity specifically for MPK6, called *S*ensor *O*f *M*APK *A*ctivity (SOMA) (Zaman et al., 2019). We used SOMA lines tagged with either the human immunodeficiency virus 1 (HIV-1) nuclear export signal (SOMA-NES) or the SV40 nuclear localization signal (SOMA-NLS) (Kalderon et al., 1984; Wen et al., 1995) to measure MPK6 activity in the cytosol or nucleus, respectively. To validate these reporters in hypocotyl epidermal cells, we quantitated FRET efficiency in the SOMA lines in response to 150 mM NaCl as a positive control (Droillard et al., 2004). FRET efficiency increased rapidly in SOMA-NES and SOMA-NLS in response to NaCl with no response observed when treated with water (Fig S6 A-D). Additionally, flg22 treatment did not cause substantial FRET efficiency changes in negative control reporter lines: $SOMA^{T679A}$-NES or $SOMA^{T679A}$-NLS, which contain mutations in the known phosphorylation site of SOMA that are necessary for FRET changes (Fig S6 E, F). As shown in Figures 6E and F, rapid FRET gains were observed in both SOMA-NES and SOMA-NLS within 2-4 minutes after treatment with flg22. When treated with 6% D-glucose, no change in FRET efficiency was observed, suggesting that D-glucose does not induce activity of MPK6 (Fig 6G and H).

To determine if CME-mediated endocytosis regulates flg22-induced MPK6 activity, we pretreated SOMA-NES lines with TyrA23. TyrA23 successfully blocked the increases in FRET efficiencies that were observed in the absence of the inhibitor (Fig 6E, replicates in Fig S6 G-N). The negative control TyrA51 showed no significant effect on FRET efficiency after treatment with flg22 (Fig S6 P-V), indicating that the inhibitory effect of TyrA23 is specific to its role in blocking CME-mediated endocytosis and suggesting that AtRGS1 endocytosis, per se, is required.

However, we do not exclude the possibility that within the context of flg22-induced MAPK signaling that some other CME-mediated step is rate-limiting.

Because D-glucose utilizes both CME and sterol-dependent pathways to induce AtRGS1 internalization, we tested if the depletion of CME pools of AtRGS1 by D-glucose would alter flg22-induced MPK6 activation. After pretreating SOMA-NES lines with D-glucose for 30 minutes prior to imaging, we found that D-glucose did not have an effect on flg22-increased FRET efficiency (Fig 6G inset) suggesting that the glucose pool of AtRGS1 is sequestered from the flg22-induced CME of AtRGS1.

We tested the role of D-glucose and flg22 in triggering an increased Ca^{2+} transient response using the intensity-based Ca^{2+} sensor R-GECO1, a red-shifted intensity-based Ca^{2+} reporter (Keinath et al., 2015). We used stable transgenic Arabidopsis lines in wild type and *rgs1-2* backgrounds expressing cytosolic- and nuclear-localized R-GECO1. For our assay, D-glucose and flg22-induced Ca^{2+} signals in wild type and *rgs1-2* plants were measured over a time course in etiolated hypocotyls and normalized against the untreated samples (Fig 6I and 6J). Ca^{2+} levels represented by fractional fluorescence changes ($\Delta F/F$; the difference between the fluorescence intensity before and after flg22 application divided by initial fluorescence intensity) increased in wild type ($p< 0.01$) while $\Delta F/F$ was greatly diminished ($\Delta F/F = \sim 0.01$) in the *rgs1*-2 mutant in response to flg22. D-glucose treatments did not significantly alter the $\Delta F/F$ in Col-0 wild type or *rgs1*-2 mutant ($p=0.62$), suggesting that D-glucose does not utilize AtRGS1 in a Ca^{2+} branch of the pathway. Despite both D-glucose and flg22 inducing AtRGS1-internalization, these results show that within this context, only flg22 is capable of inducing MPK6 activity and Ca^{2+} changes.

Here, we showed that D-glucose signaling mediated by AtRGS1 does not involve MAPK or Ca^{2+} branches, however, D-glucose has been shown to elicit a change in expression of a small

set of genes (Grigston et al., 2008; Urano et al., 2012). *TRICHOMELESS LIKE 26* (*TBL26*) is induced by glucose in an AtRGS1/G protein complex-dependent manner (Grigston et al., 2008) and has since been used as a reporter for activation (Fu et al., 2014; Urano et al., 2016; Urano et al., 2012). Paradoxically, the loss of AtRGS1 inhibits *TBL26* expression indicating that genetically, AtRGS1 is a positive modulator of signaling, contradictory to our understanding that RGS proteins negatively modulate G protein activation. One solution to this paradox is that endocytosis of AtRGS1 is required for signal propagation. To test this, we quantitated glucose-induced *TBL26* expression in the presence of TyrA23 and found that expression is dramatically reduced (Fig 6L). This is consistent with the notion that AtRGS1 signaling has an endosomal origin, analogous to some GPCRs (Eichel and von Zastrow, 2018).

DISCUSSION

The key finding in this study is system bias wherein a single receptor-like RGS protein modulates different quantifiable signaling outputs from two distinct signal inputs (Figure 7A). All of the measured signal outputs correspond to a specific ligand input. For example, flg22 induces Ca^{2+} release (Figure 6I-K) and MAPK signaling (Figure 6E-H, K) whereas D-glucose or its metabolite has a measured effect on gene expression (Figure 6L). For flg22, all members of the G protein heterotrimer, along with XLG2 and VPS26A/B are necessary for CME of AtRGS1. Additionally, specific phosphorylation of di-serines at the AtRGS1 C-terminus is required. What is interesting is that glucose signaling that transduces through the same CME of AtRGS1 also requires phosphorylation of the same di-serine residues, but not VPS26 for high dose and low duration sugar exposure (Figure 7B). This phenomenon of signaling through AtRGS1 mediated by the same mechanism of phosphorylation-dependent endocytosis with different G proteins and adapters raises the important question of how are extracellular ligands discriminated for downstream

548 signaling events? Although AtRGS1 endocytosis is necessary for G protein activation it would
549 seem that AtRGS1 is not the discriminator; rather an RLK protein that directly phosphorylates
550 AtRGS1, AtGPA1 and possibly VPS26, to provide the requisite information for ligand-specific
551 downstream signal transduction in the cell.

552 The two mechanisms of AtRGS1 endocytosis induced by D-glucose or its metabolites
553 implies that this signal-dependent pool of AtRGS1 is bipartite, prompting the question of an
554 equilibrium or steady state between the populations. The evidence so far suggests that it is not. If
555 these AtRGS1 pools were dynamically exchanging within the membrane, we would expect to
556 induce internalization of nearly all membrane bound AtRGS1 by inhibiting one mechanism of
557 endocytosis thereby causing a shift entirely to the other. For example, inhibiting CME with
558 TyrA23 would force AtRGS1 endocytosis entirely to the SDE mode, however this was not
559 observed. Inhibiting one mechanism of endocytosis only partly reduced AtRGS1 internalization
560 by half, indicating the AtRGS1 populations may be physically isolated and static in the cell
561 membrane (Figure 7C). Some AtRGS1 proteins may be grouped into so-called microdomains or
562 clusters surrounded by receptor/co-receptor RLK proteins while other AtRGS1 may be distributed
563 throughout the membrane without common neighbor RLKs (Figure 7C).

564 Similarly, the question exists whether an equilibrium between the flg22-mediated and D-
565 glucose-mediated CME pools exists and the conclusion is again that equilibria are not likely,
566 consistent with a genuine bias in signaling. To clarify, what we define as the "CME pools" here,
567 they are the portion of either the flg22- or D-glucose-activated AtRGS1 population that is inhibited
568 by TyrA23, by loss of the tyrosine binding motif, and by loss of the AP2μ subunit of the clathrin
569 complex (Figure 2). While the two pools share these properties, they do not share the requirement
570 of the candidate adapter, VPS26 monomer or dimer (Figure 4). Moreover, when the AtRGS1 pool

571 at the plasma membrane is depleted with D-glucose, there is no effect on the amplitude of flg22
572 activation (Figure 6).

573 The two mechanisms in the composite glucose-induced AtRGS1 endocytosis may be a
574 result of two distinct mechanisms of sugar perception: one through direct interaction of AtRGS1
575 with a sugar or sugar metabolite and the other through sugar binding to a RLK in the membrane
576 similar to flg22::FLS2 binding (Figure 7D). To compare and contrast these two ligand-biased
577 trajectories, the ordered steps of signal transduction from ligand perception (**step 1**) to
578 internalization of AtRGS1 (**step 5**) are enumerated in Figure 7D to illustrate mechanistically what
579 the present work revealed about each origin of endocytosis including phosphorylation (flg22- **step**
580 **2**/glucose- **step 2**), binding of our candidate adaptor VPS26 (flg22- **step 3**), formation of clathrin
581 coated vesicles (flg22- **step 4**/glucose- **step 3**), and finally endocytosis of AtRGS1 either via
582 clathrin coated vesicle (flg22- **step 5/** glucose **step 4**) or sterol dependent rafts (glucose). If glucose
583 or a metabolite is perceived by two distinct sensing mechanisms, each mechanism may operate
584 exclusively through one origin of endocytosis with a unique core of G protein and internalization
585 signaling components. Interestingly, within the glucose model, a system bias may exist favoring
586 one origin of endocytosis that results from architectural differences in the membrane surrounding
587 AtRGS1. A high density of glucose-binding RLKs may favor glucose-induced CME of AtRGS1
588 over the SDE origin.

589 The division of G protein involvement in glucose-induced CME and SDE challenges
590 previously published reports on the necessity for subunits of the G protein heterotrimer in the full
591 range of glucose signaling through AtRGS1; specifically shown was the complete abrogation of
592 AtRGS1 endocytosis in the Gβ null mutant and partial reduction of glucose-induced endocytosis
593 with the loss of Gα (Urano et al., 2012). Our results confirm that Gβ is required for AtRGS1

endocytosis, but only in a low dose scenario, 2% (~110 nM). We show no requirement for Gβ or Gα at the higher 6% (~330nm) glucose concentration. It may be that higher sugar concentrations, those typically found at or around vascular unloading areas, illicit a quicker signaling response than low dose sugar likely found in or near epidermal cells where we quantified AtRGS1 internalization. The significance of sugar signaling with regard to cell growth, division, and maintenance may necessitate multiple dose-dependent mechanisms of signal transduction encoded in different origins of endocytosis and the individual G protein associated components.

Both flg22- and D-glucose outputs require AtRGS1 (Chen et al., 2003; Grigston et al., 2008; Liang et al., 2018; Tunc-Ozdemir and Jones, 2017) and an intact heterotrimeric G protein complex (Figure 3) but as discussed for D-glucose responsiveness, the outputs depends on both the concentration and duration of D-glucose. We previously designated this non-threshold-based activation phenomenon as Dose-Duration Reciprocity (**DDR**) where a low dose of D-glucose for a long period reaches the same output amplitude as a high dose presented as a pulse (Fu et al., 2014). The proposed mechanism is recruitment of WNK8 and WNK1 to the membrane by the Gβγ dimer AGB1/AGG as a function of DDR to phosphorylate AtRGS1 for endocytosis. However, our higher resolution analyses here challenge some aspects of that mechanism and provide deeper mechanistic insight. AGB1 is essential for low D-glucose DDR but is not required for high-glucose DDR. WNK8 kinase is required as previously shown but WNK1 is shown to not be required at longer low-glucose treatments (6 hours) in contrast to previously published data (Fu, et al 2014). This discrepancy is most likely due to differences in expression level between studies (transient for Fu, et al 2014 and stable here) because glucose responsiveness is sensitive to the pool size of AtRGS1 (Liao et al., 2017).

Besides the 2 visual and 2 non-visual (aka β-) arrestins, the arrestin super family in humans also has 6 α-arrestin members. These α–arrestins have diverse functions including trafficking of non-GPCRs (Patwari and Lee, 2012) and may be closest to the ancestral arrestin from which the visual/non-visual arrestins evolved because they are found in stromenopiles basal to the opistokont lineage containing metazoans and fungi (Alvarez, 2008). Therefore, we asked whether Plantae contains α–arrestin homologs and are thus the true adaptors for trafficking plant 7TM proteins. While we found clear α–arrestin orthologs in the 4-cell alga *Tetrtabaena* (PNH03120) and in the green alga *Chara* (GBG71752), both basal to land plants, using *Mus* ARRDC3/TLIMP (BAC65781) as the search query, no hits were found in Arabidopsis (eudicot), *Amborella* (base of angiosperms), rice (monocot), and *Physcomitrella* (basal to higher land plants). This suggests that α–arrestins were lost in the plantae kingdom and this loss possibly allowed expansion of the related VPS26 family to evolve other function(s) (Alvarez, 2008).

Given the fact that many GPCR-containing organisms divergent to humans lack arrestin proteins, another important finding from this study is the suggestion that the retromer subunits AtVPS26A and B moonlight as arrestin-like adaptors for phosphorylation-induced, clathrin-dependent AtRGS1 endocytosis in Arabidopsis. Could this function be ubiquitous? Even in humans, some GPCR endocytosis occurs independently of β-arrestins yet still requires C-terminal phosphorylation, a tyrosine motif, AP2, and clathrin (e.g. (Paing et al., 2002; Smith et al., 2016)) raising the possibility that VPS26 orthologs in humans may serve the exact adaptor function for a subset of GPCRs.

This study focuses on biased signaling launched from different architectures of two AtRGS1-centered pathways. We show that phosphorylation by different sets of kinases encodes this bias. However, we have not address how the architecture is established or maintained but we

639 speculate that this too is based on a phosphorylation bar code on the AtRGS1/G protein complex.
640 Therefore, establishing the dynamics of both the pre- and post-signaling phosphorylation bar codes
641 is important for our understanding of biased system signaling.

642 Why both cytoplasmic and extracellular glucose pools are monitored by the plant cell
643 remains unclear. We speculate that the extracellular pool of glucose is far more dynamic than the
644 cytoplasmic pool due to its rapid metabolic flux in the cytoplasm compared to the apoplast.
645 Therefore, an extracellular glucose detection system may be more appropriate for monitoring
646 sugars produced by photosynthesis for real time information. This is consistent with the recent
647 finding that AtRGS1 is important for detecting fluctuations in CO_2-fixed sugar in the minute time
648 range over the diel cycle (Chen et al., 2003; Tunc-Ozdemir et al., 2018).

649 It is conceivable that this biased system sits at the crux of the "defense vs. growth trade-
650 off" dilemma that plants face. Specifically, pathogen attack compels the plant to shift its utilization
651 of fixed sugars from building cell walls to synthesizing defense molecules (Huot et al., 2014). The
652 AtRGS1/G protein complex may be the fulcrum for this balance because AtRGS1 is involved in
653 detecting fixed sugars (Mudgil et al., 2016; Tunc-Ozdemir et al., 2018), establishing cell wall
654 composition (Delgado-Cerezo et al., 2012; Escudero et al., 2017; Klopffleisch et al., 2011) and
655 serving as a sentinel in innate immunity (Zhong et al., 2018).

656 In conclusion, our data provide evidence for system biased signaling through AtRGS1 and
657 introduces a previously unknown arrestin-like adaptor. We introduce the importance of system
658 architecture as it relates to system bias in G protein complex signaling.

659

660

MATERIALS AND METHODS

Chemicals.

Methyl-β-cyclodextrin was purchased from Frontier Scientific, tyrphostin A51 and turanose were purchased from Sigma-Aldrich, and tyrphostin A23 was purchased from Santa Cruz Biotechnology. All chemicals were indicated by the vendors to be >98% pure.

Plant Growth Conditions

Arabidopsis seeds were surface sterilized with 80% EtOH for 10 seconds while vortexing followed by a 10-second vortex with 30% bleach. Seeds were subsequently washed 3X with ddH_20 and suspended in 12 well cell culture plates with ¼ MS with no sugar at pH 5.7 with 10-12 seeds per well. Plates were wrapped in aluminum foil and cold-treated at 4˚C for 2 days followed by a 2-hour light treatment to induce germination. After light treatment, plates were again wrapped in aluminum foil and placed on a horizontal shaker at ambient temperature for 5 days before imaging.

AtRGS1 Internalization Assay, Proxy for G protein activation

AtRGS1-YFP internalization was induced with D-glucose and flg22 as described (Fu et al., 2014; Tunc-Ozdemir et al., 2016; Urano et al., 2012). Briefly, wild type (Col-0) Arabidopsis seeds expressing 35S:AtRGS1-YFP were sterilized and then sown on 1-mL liquid 1/4 X Murashige and Skoog (MS) medium without sugar in 12-well plates and stratified at 5ºC for 2 days, followed by 2 hours light, then grown in darkness at RT for 3-5 days. For optimal results, the plates were kept in darkness but moved to the microscope room on the third day to acclimate. 6% D-glucose or 1µm flg22 were applied to seedlings for 30 and 10 minutes respectively before imaging. Image acquisition was done on either a Zeiss LSM710 (Zeiss Microscopy, Oberkochen, Germany) with

a C-Apochromat 40X 1.2NA water immersion objective (for figures 2A-2I and figure 3A-3D) or a Zeiss LSM880 with a C-Apochromat 40x/1.2NA water immersion objective (for figure 2K-2P, 3E-3K, and S3). YFP excitation was at 514nm and emission collection 525-565nm. Emission collection on the LSM880 was done with a GaAsP detector. For RGS internalization assays a z-stack series was acquired at 0.5µm intervals between images. Image processing and RGS internalization measurements were done with the Fiji distribution of ImageJ (Schindelin et al., 2012) as described by Urano *et al (Urano et al., 2012)* with the following modification: Internalized YFP fluorescence was measured and subtracted from total YFP fluorescence of individual cells as opposed to total fluorescence of the hypocotyl image as stated in Urano *et al*. Images were acquired on the hypocotyl epidermis 2-4 mm below the cotyledons of seedlings treated with water, glucose, and flg22 in addition to the pharmacological inhibitors. Seedling exposure to light was minimized as much as is practical while imaging to avoid light induced internalization of AtRGS1. Statistical analysis was performed using analysis of variance with n=number of cells measured. Differences in basal and treatment induced levels of RGS1-YFP internalization are a result of switching image acquisition from the LSM710 to the LSM880 to improve image resolution and accuracy of internalization measurements.

Pharmacological Inhibition of RGS Internalization

AtRGS1 internalization was inhibited with TyrA23 and MβCD under the following conditions. TyrA23 was applied to 3-day old seedlings for a pre-incubation period of 60 minutes at specified concentrations. Following the pre-incubation period, a combination of TyrA23 and 6% D-Glucose were applied to the seedlings for 30 minutes immediately followed by image acquisition. In the case of flg22, TyrA23 and 1µm flg22 were applied to the seedling for 10 minutes following the

pre-incubation period. For MβCD, the pre-incubation period was 45 minutes at specified concentrations. When both inhibitors were simultaneously applied, pre-incubation was 60 minutes

TIRF imaging and area/speed measurements of AtRGS1-GFP

Arabidopsis Col-0 seeds containing 35S-RGS1-GFP were grown as mentioned in the plant growth section. 5-day-old seedlings were transferred to a solution of either 6% D-glucose or 1µm flg22 and imaged at 5, 10, and 15 minutes while immersed in the ligand solution. Imaging was performed on a Nikon Ti Eclipse with SR Apo TIRF 100x lens (NA 1.5, WD 120µm). GFP excitation occurred at 488nm and emission collection at 515-555nm with an Andor iXon3 EMCCD camera. 60 second time-lapse imaging was initiated at the beginning of each time point with 200ms acquisition speed. Time-lapse sequences were normalized for fluorescence over time using IMARIS (v9.2.2, Bitplane AG, Zurich, Switzerland). The IMARIS Surface feature was used to track and calculate the area and speed of individually identifiable AtRGS1 proteins/clusters (labeled as tracks in IMARIS) over time. The average speed and area of each unique track for a 30 second interval between 5:15-5:45 or 15:15-15:45 was calculated using a script in Matlab (Supplemental code).

Synthesis of [^{14}C] isomaltulose

Sucrose isomerase (SI) from *Pantoea dispersa* UQ68J (GenBank AY223549) was cloned into expression vector pET24b (Novagen) first by PCR of genomic DNA using the following PCR forward primer 5'-GGA TCC AAC AAT GGC AAC GAA TAT ACA AAA GTC C-3' which included a *BamHI* restriction site and a start codon; reverse primer 5'-ATA GGT ACC TCA GTT CAG CTT ATA GAT CCC-3' which included a *KpnI* restriction site and a stop codon.

730 Expression was performed using *E. coli* BL21(DE3) (Novagen), 37°C, 225 rpm. When
731 the optical density at 600nm reached 1.00, isopropyl-D-thiogalactopyranoside was added to a final
732 concentration of 0.5 mM for induction. The incubation of the culture was continued for another 3
733 h at 28°C. Cells were harvested by centrifugation (3,000 ×g, 4°C, 10 min), resuspended in 50 mM
734 Tris-HCl (pH 8.0)-2 mM EDTA, and then re-centrifuged. The cell pellet was immediately frozen
735 in liquid nitrogen and stored at -75°C. Cells were suspended in extraction buffer (20 mM Tris-HCl
736 (pH 7.4), 200 mM NaCl, 1 mM EDTA, 1 mM azide, 10 mM β-mercaptoethanol) and then lysed
737 by sonication (nine 15-s pulses at 50 W with a Branson Sonifier 450 microprobe), centrifuged
738 (10,000 ×g, 4°C, 10 min), and filtered through a 0.45-μm-pore-size membrane (Gelman Acrodisc).
739 The pET24b vector introduced a carboxy-terminal six-His tag into expressed proteins, which were
740 purified by adsorption to nitrilotriacetic acid (NTA) agarose (QIAGEN) and elution with 25 mM
741 NaH2PO4-150 mM NaCl-125 mM imidazole buffer (pH 8.0) by following the manufacturer's
742 instructions. The purity of SI proteins was verified by SDS-PAGE as a single band on Coomassie
743 Blue R-250 staining.

744 [^{14}C] isomaltulose was prepared using 1.48MBq [U-^{14}C]Sucrose (Amersham, UK) in 200
745 μl water with 3% ethanol (equals to 0.3379 mM) was reacted with 30 μl purified UQ68J SI for at
746 30 °C 60 min. The converted [^{14}C] isomatulose concentration by UQ68J SI was estimated by three-
747 replicate parallel conversions of unlabelled sucrose (S7903,Sigma) in the same concentration of
748 0.3379 mM with 3% Ethanol by the same enzyme. BioLC DX600 (Dionex, USA) determinations
749 showed 84.0±0.106% (Mean±SE) was converted into isomaltulose, 3.5±0.197% into trehalulose;
750 into the by-products of glucose and fructose were 4.6±0.072% and 7.8±0.237% respectively and
751 there was no sucrose left after the reaction was stopped (Figure 1A).
752

Sugar uptake assay

One-week-old seedlings, grown on a filter disc overlaying 1/2X Murashige and Skoog Basal Salts, 0.7% phytogel 23ºC, pH 5.8, 8h/d of 100 mole/m2/s1, were lifted off the plate and overlaid 6 mL of water containing approx. 25,000 cpm of [^{14}C] sugars as indicated. The specific activity of the sugars was 12GBq/mmol. At the indicated times, triplicate sets of 10 seedling were gently rinsed and placed in a 1.7-mL microfuge tube with 1 mL of scintillation fluid (Perkin Elmer Inc) and radioactivity was quantitated by liquid scintillation counting. CPM from time zero (typically 80-150 cpm) was subtracted from the average of the 3 samples. The CPM for [^{14}C] isomaltulose uptake into seedlings at each time was corrected for its 84% purity. The experiment as shown was repeated once with the same result. [^{14}C] glucose uptake was repeated 4 times.

Live cell imaging of MAPK reporter (SOMA) lines

Detached etiolated hypocotyls were prepared for imaging on the confocal microscope using the HybriWell™ method as previously described (Vang et al., 2018; Zaman et al., 2019). A hypocotyl from a dark grown 5-day-old seedling was placed on top of the droplet, and a HybriWell™ (Grace BioLabs, http://gracebio.com/, cat. no. 611102) was gently placed on the coverslide with the hypocotyl in the center to form a 150-µm deep imaging chamber with a volume of 30 µl. Ultrapure water (300 µl) was injected through one of the HybriWell™ ports using a pipettor to fill the 30-µl chamber with water and to expel any air bubbles. A 200-µl droplet of ultrapure water was then placed on one of the ports to prevent the chamber from drying out. The HybriWells containing the mounted hypocotyls were then placed in covered Petri dishes and equilibrated by incubating at 20–23°C under constant light for 6–8 hours prior to imaging.

775 Confocal microscopy was performed using a Zeiss LSM 710 with a C-Apochromat
776 40x/1.20 water immersion objective lens. Samples were excited at 458nm with 3% power, and
777 emission was measured between 463 and 517nm for Turquoise GL and between 534 and 570nm
778 for YPet. Z-stacks were collected every 2 min with an optical slice thickness of 1.2 µm. Chemical
779 treatments were added to the samples during imaging by pipetting 200 µl of solution containing
780 the treatment onto one port of the HybriWell. For experiments involving tyrphostin A23 and
781 tyrphostin A51, hypocotyls were pretreated with 50 µM of these compounds for 30 min prior to
782 imaging.

783 Post-processing of the raw image data was performed using Fiji (Schindelin et al., 2012).
784 The 'Z-projection' function was performed on an image stack using the 'Max Intensity' setting.
785 The resulting projection was then separated into two images, one for the Turquoise GL emission
786 channel and one for the YPet emission channel. The 'Subtract Background' function was
787 performed on both images, with the 'rolling-ball radius' set as the default 50 pixels. A mask was
788 then created from the YPet channel using the 'Convert to Mask' function. The background
789 subtracted YPet and Turquoise GL images were then converted into 32-bit images. These 32-bit
790 images were then multiplied by the Mask file. The resulting YPet image was divided by the
791 resulting Turquoise GL image using the 'Image Calculator' function to create a ratio image
792 representing the ratio of YPet to Turquoise emission. Finally, the 'Threshold' function was
793 performed using the default values, with the 'NaN background' option enabled. The 'Fire' lookup
794 table was then applied to the final ratio image. To measure the ratio of YPet to Turquoise GL
795 emission, a region of interest (ROI) was selected within the ratio image using Fiji and the average
796 ratio value within that ROI was then measured.

797 *Live cell Ca^{++} imaging with R-GECO1*

798 5-day-old etiolated hypocotyls expressing R-GECO1 calcium reporter were grown in aqueous
799 media containing ¼ MS. Hypocotyls were excised and mounted in HybriWells 6-8 hours prior to
800 imaging with a Zeiss LSM710 confocal laser scanning microscope equipped with a C-Apochromat
801 40×/1.20 water immersion objective. R-GECO1 was excited using 561nm laser with 7.0 % laser
802 power, and emission was measured between 620 and 650 nm. Z-stacks were collected 2 min after
803 chemical treatment with an optical slice thickness of 1.5µm. Chemical treatments were added to
804 the samples during imaging by pipetting 200 µl of solution containing the treatment onto one port
805 of the HybriWell. The digital images were analyzed with Fiji (Schindelin et al., 2012).

806 *Modeling AtVPS26*

807 Five models (atvps26a1-5) were created by the MODELLER using the automodel script based on
808 the human VPS26A template 2FAU. For evaluation and selection of the "best" model, we
809 calculated the objective function (molpdf), Discrete Optimized Protein Energy (**DOPE**) score,
810 GA341 assessment score and root mean square deviation (**RMSD**) between the model and the
811 template. The best model has the lowest value of the molpdf and overall DOPE assessment scores.
812 In addition, DOPE scores were calculated per-residue and the template and the five atvps26a
813 models were compared using GNUPLOT (Figure S4C) and found to be dissimilar in only three
814 positions (residue around 60, 240, and 260). The atvps26a2 model was selected based on the
815 lowest, RMSD value (Figure S4D) and plotted DOPE per-residue score curve (Fig. S4E). With an
816 RMSD of 0.17 Å, atvps26a-2 differs from the template by less than the length of a C-C bond.

817 *Split firefly luciferase assays*

818 pCAMBIA/des/cLuc and pCAMBIA/des/nLuc (Lin et al., 2015) were used to generate the
819 following plasmids: AtVPS26A-nLUC, AtVPS26B-nLUC, cLUC-AtVPS26A, cLUC-AtVPS26B,
820 cLUC-AtVPS26like, cLUC-AtGPA1, AtAGB1-nLUC and AtRGS1-nLUC. pART27H-mCherry-

AtAGG1 plasmid was obtained from Dr. Jose R Botella (University of Queensland, Brisbane, QLD, 4072, Australia). All plasmids were transformed into *A. tumefaciens* strain *GV3101*. nLUC and cLUC fusion partners were co-expressed in *N. benthamiana* leavesby agroinfiltration following protocols in (Zhou et al., 2018). 48 hours after infiltration, 6mm Leaf discs were collected to 96-well plate and 40µl 0.4mM D-luciferin was added to each well. Luminescence was measured by spectraMax L microplate reader (Molecular Devices).

Yeast two-hybrid assays

Constructs used in yeast two-hybrid assays were pAS–RGS-J5 (amino acids 284–459), RGS-ΔCt (amino acids 284–416), RGS-ΔCtS405,406A, pACTGW–AtVPS26B and AtVPS26like. Y2H tested pairs were co-transformed into *AH109* yeast cells and plated on SD-LW media (Wagemans and Lavigne, 2015). Colonies were then inoculated into SD-LW liquid media and grew overnight at 30 °C. Then 1/10 diluted yeast cells were spotted on SD-LW, SD-LWH, and SD-LWH 10mM 3-AT (3-amino-1,2,4-triazole) plates. The plates were incubated at 30°C for 4 days and were imaged by gel documentation system (Axygen) under white light.

SUPPLEMENTAL INFORMATION

Supplemental Information includes 6 figures and 1 text file.

ACKNOWLEDGEMENTS

We would like to thank Dr. N Phan for creating the AtRGS1^{Y112A} plasmid and transgenic lines and for experiments testing the involvement of adaptors in AtRGS1 endocytosis and data in Figure 1A and B. We thank Dr. V Gurevich, Dr. M Garcia-Marcos and Dr. CE Alvarez for helpful comments and Dr. K Ghusinga for assistance with writing MatLab code. We thank Dr. J Huang for help in

the turanose experiment. This work was supported by grants from the NIGMS (GM065989) and NSF (MCB-1713880) to A.M.J. The Division of Chemical Sciences, Geosciences, and Biosciences, Office of Basic Energy Sciences of the US Department of Energy through the grant DE-FG02-05er15671 to A.M.J. funded the biochemical aspects of this project. The content is solely the responsibility of the authors and does not necessarily represent the official views of the National Institutes of Health.

AUTHOR CONTRIBUTIONS

T.J.R-E., J.W., X.S., B.D., H.J., J.Y., M.T-O, F.L. and A.M.J. performed experiments and produced data used in the figures. T.J.R-E., J.W., X.S., and A.M.J. designed experiments, and analyzed results. P.K provided the MAPK reporters prior to its publication and guided those experiments. L.W. synthesized and purified [^{14}C]isomaltulose. Y.T. performed sugar uptake experiments shown in Figure 1. T.J.R-E., J.W., and A.M.J wrote the paper.

DECLARATION OF INTERESTS

The authors declare no competing interest.

862 **Figure legends**
863
864 **Figure 1. AtRGS1 perceives extracellular glucose or glucose metabolite**. While flg22 is
865 perceived extracellularly, an extracellular site of glucose perception for activation of G signaling
866 in Arabidopsis has not yet been made with an impermeant glucose analog. See supporting data
867 for this figure in Supplemental Material Figure S1. **A**. Isomaltulose and D-glucose induce rapid
868 AtRGS1-YFP endocytosis in a dose-dependent manner. Images are representative from hypocotyl
869 epidermal cells ectopically expressing AtRGS1 tagged with YFP. **B**. Despite being 9-fold less
870 permeant to the Arabidopsis plasma membrane, isomaltulose is slightly more potent than D-
871 glucose in activation of G signaling as measured by proxy using AtRGS1-YFP endocytosis (Fu et
872 al., 2014). **C**. Turanose is impermeant to plant cells (Rolland et al., 2002) yet is as effective as D-
873 glucose in inducing AtRGS1-YFP endocytosis. The purity of turanose was >98%. **D**. Structures.
874 Both isomaltulose and turanose share a glucose ring moiety.
875
876 **Figure 2. Two origins of AtRGS1 endocytosis.** Pharmacological inhibitors show two origins of
877 AtRGS1-YFP endocytosis. (**A**) AtRGS1-YFP seedlings were treated with increasing
878 concentrations of MβCD at 0mM (n= 18 (flg22) and 15 (glucose)), 1mM (n= 14 and 14), 2mM
879 (n= 15 and 16), 5mM (n= 17 and 14), 10mM (n= 12 and 17), and 20mM (n= 15 and 6) for 45 min
880 followed by incubation in the same solution but supplemented with 1 μM flg22 for 10 min or (**B**)
881 6% D-glucose for 30 min before imaging epidermal cells. Internalized AtRGS1-YFP was
882 quantified to determine total endocytosis of AtRGS1. MβCD does not inhibit flg22-induced
883 AtRGS1 endocytosis, but does partially inhibit glucose-induced AtRGS1 endocytosis at 5mM and
884 above ($p<0.01$). (**C**) TyrphostinA23, an inhibitor of CME, significantly impairs flg22-induced
885 AtRGS1 endocytosis (n=14) and (**D**) partially inhibits glucose-mediated AtRGS1 endocytosis

886 (n=27) ($p<0.01$). The structurally similar, but inactive analog of TyrA23, TyrA51, has no effect
887 (n=19) indicating the effect of TyrA23 is specific. (**E**) When both inhibitors are applied with
888 glucose, AtRGS1 internalization is reduced to basal levels (n=8) ($p<0.01$). A genetics approach to
889 inhibit AtRGS1 internalization confirms pharmacological results. (**F**) A genetic null mutant of
890 *ap2μ*, the cargo recognition complex for CME, results in complete inhibition of flg22-induced
891 AtRGS1 (n=16) ($p<0.01$) down to basal levels, confirming TyrA23 results. (**G**) Glucose-induced
892 internalization of AtRGS1 is partially inhibited in the *ap2μ* mutant (n=32) ($p<0.01$), but further
893 reduced to basal levels with the addition of MβCD (n=18) ($p<0.01$). (**H**) Mutation of Y^{112} to
894 Alanine in the AtRGS1 tyrosine motif recognized by ap2μ, $AtRGS1^{Y112A}$, inhibits flg22-induced
895 AtRGS1 endocytosis to basal levels (n=16) ($p<0.01$). (**I**) Glucose-mediated AtRGS1 endocytosis
896 is partially inhibited in $AtRGS1^{Y112A}$ (n=12) ($p<0.05$), but subsequently reduced to basal levels
897 with the addition of MβCD (n=9) ($p<0.01$). Quantification of AtRGS1-YFP fluorescence is
898 discussed in methods. (**J**) The speed and surface area of AtRGS1-GFP particles as tracked and
899 measured by IMARIS from 30 second time lapse imaging using TIRF at 5 minutes after treatment
900 with glucose and flg22. Identifiable AtRGS1-GFP particles are significantly smaller in the flg22
901 treated population (n=2026) compared to glucose (n=4619). No significant difference in speed is
902 observed between particles in the two treatments. (**K-P**) Endocytosis markers CLC-mCherry and
903 FLOT1-mCherry localize to the cell periphery and increase overlap with RGS1-GFP in a ligand
904 dependent manner after treatment with flg22 and glucose. Zeiss confocal micrographs show
905 AtRGS1-GFP (**green channel**) and either CLC-mCherry (**red channel K-M**) or FLOT1-mCherry
906 (**red channel N-P**) after 5 minute treatments with water (**K and N**), flg22 (**L and O**), and glucose
907 (**M and P**). After water treatment, CLC-mCherry (**K box inset**) and FLOT1-mCherry (**N box**
908 **inset**) remain distributed throughout the cell cytoplasm and highly overlapped AtRGS1-GFP

particles (**Q**). After treatment with flg22, CLC-mCherry migrates to the cell periphery with an observed increase in protein agglomeration (**L red arrows**) and decrease overlap score with RGS1GFP (**S**), while FLOT1-mCherry has no observable change compared to water (**G box inset and R**). Upon treatment with glucose, FLOT1-mCherry protein bodies congregate at the cell periphery (**P red arrows**) and decrease overlap with RGS1-GFP (**V**) , while CLC-mCherry remains unchanged compared to water (**M box inset and U**). (**W**) The average overlap scores for CLC-mCherry and FLOT1-mCherry after addition of water (n= 8 and 9), flg22 (n= 4 and 7), and glucose (n= 4 and 3). flg22 addition induces a significant change in CLC compared to glucose and water while glucose induces a significant change with FLOT1 compared to flg22 and water ($p<0.01$).

Figure 3. CME of AtRGS1 is phosphorylation dependent and G protein monomer specific. Known phosphorylation sites at serine residues on the C-terminal end of AtRGS1 are required for both flg22 and glucose-induced CME of AtRGS1. (**A**) A truncated AtRGS1, AtRGS1$^{\Delta Ct}$, lacking the 43 most C-terminal residues, including 8 serines, resulted in basal levels of flg22-induced AtRGS1 internalization (n=11) ($p<0.01$). (**B**) Glucose-induced AtRGS1 internalization is partially reduced in AtRGS1$^{\Delta Ct}$ (n=12) ($p<0.01$), but further reduced to basal levels with the addition of MβCD (n=13) ($p<0.01$). (**C and D**) Mutation of three specific serine residues to alanine at 428, 435, and 436, in a full length AtRGS1, AtRGS1^{3SA}, yielded similar results to AtRGS1$^{\Delta Ct}$ for flg22 (n=10) and glucose-mediated internalization (n=22) ($p<0.01$), but indicate phosphorylation of one or several specific serine residues is necessary for CME of AtRGS1. flg22 and glucose require known kinases for AtRGS1 internalization. (**E**) Genetic ablation of the flg22 receptor FLS2 yields basal levels of flg22-induced AtRGS1 internalization (n=12) ($p<0.01$), but does not affect glucose-

induced AtRGS1 internalization (n=9). (**F**) Similarly, null mutation of the BAK1 co-receptor, *bak1-4*, results in ablated flg22-induced AtRGS1 internalization (n=16) ($p<0.01$), but not for glucose (n=17) ($p=0.36$). (**G**) The high dose and low duration glucose specific WNK8 kinase is necessary for glucose induced AtRGS1 internalization (n=13) ($p<0.01$), but not flg22 (n=10) ($p=0.9$). Individual G proteins are necessary for AtRGS1 endocytosis in a ligand specific manner. (**H**) A genetic null mutant of Gα, *gpa1-4*, limits flg22-induced endocytosis of AtRGS1 to basal levels (n=15), while glucose-induced endocytosis is unaffected compared to wild-type (n=22). (**I**) A null mutation of XLG2, *xlg2-1*, an extra-large Gα protein, also reduced flg22-induced AtRGS1 endocytosis to basal levels (n=14), but had no significant effect on glucose-mediated endocytosis compared to wild type (n=19) ($p<0.01$). (**J**) A null mutation of the AGB1/AGG1 heterodimer, *agb1-2/agg1*, inhibited flg22-induced AtRGS1 endocytosis (n=15), but had no effect on high dose, low duration glucose-induced AtRGS1 endocytosis (n=17) ($p<0.01$). (**K**) At low dose, long duration AGB1/AGG1 are necessary for glucose induced internalization (n=25). Quantification of AtRGS1-YFP fluorescence is discussed in methods.

Figure 4. Arabidopsis VPS26 subunits of the retromer complex may moonlight as arrestin-like adaptors for AtRGS1 internalization. (**A)** 3-D alignment of the model atvps26a-2 (colored cyan) with the bovine arrestin-3 (PDB 3P2D, (colored wheat). The structure of model atvps26a-2 shows a similar arrestin scaffold with arrestin-3 which contains a semi-symmetric fold of two β strand sandwich structures in the N domain and C domains linked by the central loops (ii); each sandwich is formed by 3 or 4 β sheets, respectively. (**B)**. Differences between atvps26a-2 model and bovine arrestin-3. Model atvps26a-2 lacks a short α-helix (i) inside the arrestin N-terminal domain which has been implicated in receptor binding. Arrestin-3 contains a longer C terminal tail

955 which extend all the way to bind the N terminal domain which is important for clathrin-mediated
956 endocytosis (CME) in animals. The C terminus of atvps26a-2 has no extension. (**C**). The central
957 crest. The central crest of atvps26a is similar with that of arrestin-3 which includes the finger loop,
958 middle loop and the C loop, although arrestin-3 has a longer finger loop which is important for
959 receptor binding. (**D, E**) The polar core of bovine arrestin-3.The residues in the polar core of
960 arrestin-3 are Asp_{27}, Arg_{170}, Asp_{291}, Asp_{298} and Arg_{393} which are shown as vacuum electrostatics
961 (**D**) and sticks (**E**). (**F,G**) The polar core of atvps26A. The residues of atvps26a are the N domain
962 residues Glu_{118} and Tyr_{120}, and C domain residues Arg_{213}, Glu_{215}, Thr_{258}, Tyr_{272}, and Arg_{296} which
963 are also shown as vacuum electrostatics (**F**) and sticks (**G**). Although different amino acid
964 composition, both cores consist of similarly-positioned, positive-charged residues and allow the
965 formation of hydrogen bonds under physiological conditions. However, the orientation and shape
966 of the polar core of atvps26a-2 is distinct from arrestin-3. The arrestin-3 polar core is embedded
967 between β sheets in the N terminal domain whereas the atvps26a-2 core is open and elongated,
968 spanning the length of space between the N domain and C domain.
969
970 **Figure 5. Physical interaction between AtRGS1 and VPS26.** (**A**) Bifluorescence
971 complementation (BiFC) of VPS26A and VPS26B showing a specific head-to-tail orientation
972 requirement. Representative cells shown. n=5. Experiment repeated 2 times. (**B**) Split luciferase
973 complementation by VPS26A and VPS26B heterodimers and VPS26B homodimers. Error bars
974 are standard error of the mean (SEM). Means with different letters indicate significantly different
975 (Tukey's HSD test, $p<0.05$). n=64 leaf discs from 4 individual tobacco plants. (**C**) BiFC of VPS26
976 A and VPS26B with AtRGS1 in a specific orientation. (**D**) Split-luciferase complementation by
977 VPS26A and AtRGS1. Positive control is complementation by the heterotrimeric G protein

978 complex (GPA1/AGB1/AGG1). Negative control is AtGPA1 and AGB1 in the absence of AGG1.
979 Error bars are SEM. n=64. ($p<0.05$). (**E**) Yeast two-hybrid complementation between the
980 cytoplasmic domain of AtRGS1 (RGS1-J5) and VPS26B. RGS1-J5 contains the linker between
981 the 7TM domain and the RGS box, the RGS box and a C-terminal tail (CT). RGS1- ΔCT lacks the
982 C-terminal tail which contains the phosphorylation cluster required for AtRGS1 endocytosis.
983 RGS1- $\Delta CTS_{405,406A}$ lacks the CT and has two additional phosphosites mutated. –LW is the
984 leucine/tryptophan dropout, -LWH is the leucine/tryptophan/histidine drop out media; 10 mM 3-
985 AT indicates higher stringency by the addition of 10 mM 3-amino-1,2,4-triazole.

986

987 **Figure 6. MAPK activation and Ca^{2+} signaling in response to flg22 and D-glucose.** (**A-D**)
988 Processed confocal images of the epidermis of etiolated hypocotyls from the SOMA-NLS (**A, B**)
989 and SOMA-NES (**C, D**) transgenic lines depicting the ratio of YPet to Turquoise GL emission
990 produced by exciting Turquoise GL. Scale bar represents 100 µm. Time stamps indicate when the
991 image was collected labeled minutes:seconds. Images at 00:00 were collected before treatment,
992 while those at time point 20:00 were collected 5 minutes after treatment with 1 µM flg22. White
993 rectangle represent regions of interest (ROIs) used to measure YPet and Turquoise GL emission.
994 (**E-H**). The ratio of YPet to Turquoise GL emission produced by exciting Turquoise GL over time
995 was determined using the ROIs shown in (A-D). During the first 10 minutes of each experiment
996 the samples were incubated in water. The arrow indicates the time at which 1 µM flg22 (**E, G**) or
997 6% D-glucose (**F, H**) was added to the sample. (**E**) SOMA-NES lines pretreated with water
998 (orange) or 50 µM TyrA23 (yellow) prior to imaging. Inset graph (**F**) shows SOMA-NES line
999 pretreated with 6% D-glucose for 30 minutes prior to imaging. (**I**) flg22 dose-response in SOMA-
1000 NES lines. flg22 was added after two minutes of imaging. (**J, K**) R-GECO1 lines treated with

1001 flg22 or D-glucose in Col-0 (**J**) or *rgs1-2* (**K**) backgrounds. Fluorescence intensity changes of R-
1002 GECO1 in ~20 regions of interests in wild type plants. Fractional fluorescence changes (ΔF/F) for
1003 R-GECO1 were calculated from background corrected intensity values of R-GECO1 as (F −
1004 F0)/F0, where F0 represents the average fluorescence intensity of the baseline of a measurement
1005 of each genotype. Error bars are standard deviations. Asterisks represent statistical significance (*P*
1006 < 0.01) between treatment and water as determined by 2-way ANOVA.
1007
1008 **Figure 7. Component overview of flg22- and D-glucose-biased signaling. (A)** Simple model
1009 illustrating flg22 and glucose or metabolite input and the respective bias signaling output through
1010 AtRGS1, as well as a chart summary detailing the origins of endocytosis (CME and SDE),
1011 recognition motif and phosphorylation requirements, and individual proteins necessary for
1012 glucose- and flg22-induced endocytosis of AtRGS1. (**B**) Membrane overview illustrating proposed
1013 AtRGS1 microdomain clusters with common RLK neighbors. flg22 (orange circle) binds to FLS2
1014 to initiate signaling through AtRGS1. The mechanism of glucose (blue circle) perception is
1015 unknown as indicated by the question marks. After ligand perception, SDE or CME of AtRGS1
1016 occurs to permit downstream signaling. (**C**) A diagram of the individual components involved in
1017 the mechanism of endocytosis initiated by flg22 and glucose or metabolite. Numbers indicate the
1018 order of operations. For flg22: (1) perception of ligand, (2) phosphorylation of AtRGS1 by a RLK,
1019 (3 and 4) binding of clathrin complex and/or VPS26 in an unknown order, and (5) internalization
1020 of AtRGS1. For glucose or metabolite: (1) ligand perception by a RLK or direct interaction with
1021 AtRGS1, (2) receptor interaction with WNK kinase (in the case of SDE, #2 indicates immediate
1022 endocytosis because other key components of the pathway are unknown), (3) phosphorylation of
1023 AtRGS1 by WNK kinases, (4) binding of clathrin complex to AtRGS1, and (5) internalization of

AtRGS1. TyrA23 is shown inhibiting CME in both pathways, while MβCD is shown inhibiting AtRGS1 microdomain formation at the membrane.

Supplemental Information

Supplemental Figure S1. **Isomaltulose is nearly impermeant in Arabidopsis**. **A**. To test the permeability of Arabidopsis seedlings to isomaltulose, [^{14}C] isomaltulose was synthesized and purified to 84% as described in the methods. Sugar analysis is as described and the results shown. **B**. Uptake of [^{14}C] D-glucose and [^{14}C] isomaltulose into Arabidopsis seedlings was tested. AU, Arbitrary Units as described.

Supplemental Figure S2. Tracking AtRGS1 after ligand addition. (**A-E**) IMARIS surface tracking showing (**A**) the original wide-field image acquired by TIRF, (**B**) the tracked spots imposed on the original image and tracked at (**C**) 15s, (**D**) 30s, and (**F**) 60s after initiating time-lapse imaging. (**F-H**) Tracking results showing the (**F**) average speed and area for AtRGS1-GFP particles after addition of (**x**) flg22 and (**o**) glucose at 15 minutes post ligand addition. (**G**) area and (**H**) speed of AtRGS1-GFP particles are broken out into proportion of total tracked particles at 15 minutes post ligand addition. (**I-T**) Original field of view confocal micrographs highlighting areas used to calculate Manders Overlap Coefficients from Figure **2K-P** (white and yellow boxes) with the addition of 15 minute post ligand addition images.

Supplemental Figure S3. G protein involvement in low dose, long duration sugar signaling (**A**) 2% glucose addition for 6 hours to the genetic null mutant *wnk1-1* shows no discernable difference in AtRGS1 internalization compared to wild type (n=16) ($p<0.01$). (**B**) XLG2 is not necessary for AtRGS1 internalization with low-glucose DDR (n=18) ($p<0.01$).

Figure S4. Supplemental data used to create the VPS26 model and comparison with arrestin structure described in main figure 4. (**A**) Homogeneous sequence alignment of VPS26 family (Arabidopsis VPS26a, VPS26b, VPS26like and Human VPS26A, VPS26B) with arrestin family (Human arrestin-1, arrestin-2 and bovine arrestin-1, arrestin-2, arrestin-3, squid arrestin-1, shrimp arrestin-1)**.** (**B**) The identity matrix between arrestin family and VPS26 family. Clustal Omega https://www.ebi.ac.uk/Tools/msa/clustalo/ was used to generate the Multiple Sequence Alignment file and the identity matrix result. Then the ESPript 3.0 (Easy Sequencing in PostScript) which is a program which renders sequence similarities and secondary structure information from aligned sequences for analysis and publication purpose is used to generate the final alignment file http://espript.ibcp.fr/ESPript/ESPript/index.php. A percentage of equivalent residues is calculated per columns, considering physicochemical properties. A global score is calculated for all sequences by extracting all possible pairs of residues per columns, for the score greater than similarity GlobalScore (0.7), it was rendered as colored characters (red characters on a white background and white characters on a red background if residues are strictly conserved in the column) with blue frames. AtVPS26A has a high sequence identity of 91.06% with AtVPS26B and a 56.48% sequence identity with human VPS26A (shown in red box in figure B). AtVPS26A and the arrestin family share 14-20% sequence identity (shown in red box in the figure). Sequences: 1. DpArr1, squid arrestin-1; 2. p44, bovine arrestin-1 splice variant; 3. BtArr3, Bovine

Arrestin-3; 4. PmArr1, shrimp arrestin-1; 5. BtArr1, Bovine Arrestin-1; 6. HsArr1, Human Arrestin-1; 7. BtArr2, Bovine Arrestin-2; 8. HsArr2, Human Arrestin-2; 9. AtVPS26like, Arabidopsis VPS26like; 10. AtVPS26A, Arabidopsis VPS26A; 11. AtVPS26B, Arabidopsis VPS26B; 12. HsVPS26A, human VPS26A; 13. BtVPS26A, bovine VPS26A; 14. HsVPS26B, human VPS26B; 15. BtVPS26B, bovine VPS26B.) (**C**) Model evaluation results of the 5 models of AtVPS26A. The MODELLER objective function (molpdf), DOPE assessment scores (Discrete Optimized Protein Energy, which is a statistical potential used to assess homology models in protein structure prediction), GA341 assessment score (range from 0.0 (worst) to 1.0 (native-like)) and RMSD (root-mean-square deviation, Å) with the template were calculated to evaluate the models. The "best" model is selected with the lowest value of the molpdf, DOPE score and RMSD value. The second model (atvps26a-2) was selected given the best DOPE score and RMSD value. (**D**) DOPE per residue score files of the 5 atvps26a models and the template. DOPE per residue score files of the five atvps26a models and the template human VPS26A[2FAU] were plotted using GNUPLOT which is a portable command-line driven graphing utility http://www.gnuplot.info/. Upper panel is the curves of the five atvps26a models and the template. The lower panel is the curve of the "best" model atvps26a-2 with the template. (**E**) 3D-structural alignment between model atvps26a-2 with human VPS26a template (PDB [2FAU]). atvps26a-2 model colored in pale-cyan and human VPS26A template colored in bright-orange using pymol. Upper panel: Side view. Lower panel: Top view. (**F**) Etiolated hypocotyls of Col-0 and VPS26 null mutants at 5 days old, the age used for experiments in Figure 5. Seedlings were germinated and grown in liquid MS for 5 days and transferred to solid agar plates for imaging. Scale bar 5mm.

Supplemental Figure S5. Positive and negative controls for SOMA markers. (**A-D**) (**A**) Transgenic lines SOMA-NLS (Nuclear MAPK reporter) and (**B**) SOMA-NES (cytoplasmic MAPK reporter) were analyzed before and after treatment with 150 mM NaCl as a positive control and with water (**C** and **D**) as the negative control. (**E,F**) Negative control reporters: Mutants of the transgenic lines SOMA^{T679A}-NLS (**E**) and SOMA^{T679A}-NES (**F**) were treated with 1 µM flg22. (**G - O**) Replicate experimental tracings showing reproducibility of TyrA23 inhibition of the flg22-induced activation of G signaling via AtRGS1-YFP internalization (**G - N**) and its corresponding TyrA51 negative control (**O - V**). During the first 10 minutes of each experiment, SOMA-NES lines pretreated with 50 µM TyrA23 for 10 min (**G - N**) or 50 µM TyrA51 (**O - V**) for 30 minutes prior to activation with flg22. Each graph represents 1 individual hypocotyl and each trace is a region of interest. (**W**) SOMA-NES was pretreated with 6% D-glucose for 30 minutes prior to analysis. Hypocotyls were then treated with 1 µM flg22.

Supplemental Figure S6. Positive and negative controls and dose response. Transgenic lines SOMA-NLS and SOMA-NES were analyzed before and after treatment with 150 mM NaCl as a positive control (**A**, **B**) and water (**C**, **D**). (**E**, **F**) Mutants of the transgenic lines SOMA^{T679A}-NLS and SOMA^{T679A}-NES were treated with 1 µM flg22 during the first 10 minutes of each experiment the samples. SOMA-NES lines were pretreated with 50 µM TyrA23 (**G**-**N**) or 50 µM TyrA51 (**O**-**V**) for 30 minutes prior to imaging. (**W-AB**) flg22 dose-response in SOMA-NES lines. (**AC**-**AH**) flg22 dose-response in R-GECO1 lines. Each graph represents 1 individual hypocotyl.

Supplemental Code. MatLab code for averaging unique tracked AtRGS1 particle speed and area. Speed and area data from IMARIS is exported in xls format and imported to MatLab for

sorting. Each AtRGS1 tracked protein or cluster has a unique trackID that is sorted while maintaining association with speed and area at defined time points. We identified the start and end location for each unique trackID and created a matrix to store the data and subsequently find the mean for speed and area within our defined time points.

REFERENCES

Adam, T., Bouhidel, K., Der, C., Robert, F., Najid, A., Simon-Plas, F., and Leborgne-Castel, N. (2012). Constitutive expression of clathrin hub hinders elicitor-induced clathrin-mediated endocytosis and defense gene expression in plant cells. FEBS Letters *586*, 3293-3298.

Allen, J.A., Yost, J.M., Setola, V., Chen, X., Sassano, M.F., Chen, M., Peterson, S., Yadav, P.N., Huang, X.-p., Feng, B., *et al.* (2011). Discovery of β-arrestin–biased dopamine D_2 ligands for probing signal transduction pathways essential for antipsychotic efficacy. Proceedings of the National Academy of Sciences *108*, 18488-18493.

Alvarez, C.E. (2008). On the origins of arrestin and rhodopsin. BMC Evolutionary Biology *8*, 222.

Asai, T., Tena, G., Plotnikova, J., Willmann, M.R., Chiu, W.-L., Gomez-Gomez, L., Boller, T., Ausubel, F.M., and Sheen, J. (2002). MAP kinase signalling cascade in Arabidopsis innate immunity. Nature *415*, 977-983.

Banbury, D.N., Oakley, J.D., Sessions, R.B., and Banting, G. (2003). Tyrphostin A23 inhibits internalization of the transferrin Receptor by perturbing the interaction between tyrosine motifs and the medium chain subunit of the AP-2 adaptor complex. J Biol Chem *278*, 12022-12028.

Bandyopadhyay, A., Van Eps, N., Eger, B.T., Rauscher, S., Yedidi, R.S., Moroni, T., West, G.M., Robinson, K.A., Griffin, P.R., Mitchell, J., *et al.* (2018). A novel polar core and weakly fixed C-tail in squid arrestin provide new insight into interaction with rhodopsin. Journal of Molecular Biology *430*, 4102-4118.

Bashline, L., Li, S., Anderson, C.T., Lei, L., and Gu, Y. (2013). The endocytosis of cellulose synthase in Arabidopsis Is dependent on μ2, a clathrin-mediated endocytosis adaptin. Plant Physiology *163*, 150-160.

Benovic, J., Kuhn, H., Weyand, I., Codina, J., Caron, M., and Lefkowitz, R. (1987). Functional desensitization of the isolated beta-adrenergic receptor by the beta-adrenergic receptor kinase: potential role of an analog of the retinal protein arrestin (48-kDa protein). Proceedings of the National Academy of Sciences of the United States of America *84*, 8879 - 8882.

Benovic, J.L., Strasser, R.H., Caron, M.G., and Lefkowitz, R.J. (1986). Beta-adrenergic receptor kinase: identification of a novel protein kinase that phosphorylates the agonist-occupied form of the receptor. Proceedings of the National Academy of Sciences *83*, 2797-2801.

Bohn, L.M., Gainetdinov, R.R., Lin, F.-T., Lefkowitz, R.J., and Caron, M.G. (2000). μ-Opioid receptor desensitization by β-arrestin-2 determines morphine tolerance but not dependence. Nature *408*, 720-723.

Börnke, F., Hajirezaei, M., Heineke, D., Melzer, M., Herbers, K., and Sonnewald, U. (2002). High-level production of the non-cariogenic sucrose isomer palatinose in transgenic tobacco plants strongly impairs development. Planta *214*, 356-364.

Boucrot, E., Saffarian, S., Zhang, R., and Kirchhausen, T. (2010). Roles of AP-2 in clathrin-mediated endocytosis. PLoS One *5*, e10597.

Butcher, A.J., Prihandoko, R., Kong, K.C., McWilliams, P., Edwards, J.M., Bottrill, A., Mistry, S., and Tobin, A.B. (2011). Differential G-protein-coupled receptor phosphorylation provides evidence for a signaling bar code. Journal of Biological Chemistry *286*, 11506-11518.

Charest, P.G., Oligny-Longpré, G., Bonin, H., Azzi, M., and Bouvier, M. (2007). The V2 vasopressin receptor stimulates ERK1/2 activity independently of heterotrimeric G protein signalling. Cellular Signalling *19*, 32-41.

Chen, J.-G., Willard, F.S., Huang, J., Liang, J., Chasse, S.A., Jones, A.M., and Siderovski, D.P. (2003). A seven-transmembrane RGS protein that modulates plant cell proliferation. Science *301*, 1728-1731.

Chen, L.-Q., Hou, B.-H., Lalonde, S., Takanaga, H., Hartung, M.L., Qu, X.-Q., Guo, W.-J., Kim, J.-G., Underwood, W., Chaudhuri, B.*, et al.* (2010). Sugar transporters for intercellular exchange and nutrition of pathogens. Nature *468*, 527.

Chen, Q., Iverson, T.M., and Gurevich, V.V. (2018). Structural basis of arrestin-dependent signal transduction. Trends in Biochemical Sciences *43*, 412-423.

Chen, Q., Zhuo, Y., Kim, M., Hanson, S.M., Francis, D.J., Vishnivetskiy, S.A., Altenbach, C., Klug, C.S., Hubbell, W.L., and Gurevich, V.V. (2014). Self-association of arrestin family members. In Arrestins - Pharmacology and Therapeutic Potential, V.V. Gurevich, ed. (Berlin, Heidelberg, Springer Berlin Heidelberg), pp. 205-223.

Chinchilla, D., Bauer, Z., Regenass, M., Boller, T., and Felix, G. (2006). The *Arabidopsis* receptor kinase FLS2 binds flg22 and determines the specificity of flagellin perception. The Plant Cell *18*, 465-476.

Choi, M., Staus, D.P., Wingler, L.M., Ahn, S., Pani, B., Capel, W.D., and Lefkowitz, R.J. (2018). G protein–coupled receptor kinases (GRKs) orchestrate biased agonism at the β₂-adrenergic receptor. Science Signaling *11*, eaar7084.

Collins, B.M., McCoy, A.J., Kent, H.M., Evans, P.R., and Owen, D.J. (2002). Molecular architecture and functional model of the endocytic AP2 complex. Cell *109*, 523-535.

DeFea, K.A., Zalevsky, J., Thoma, M.S., Déry, O., Mullins, R.D., and Bunnett, N.W. (2000). β-Arrestin–dependent endocytosis of proteinase-activated receptor 2 is required for intracellular targeting of activated Erk1/2. The Journal of Cell Biology *148*, 1267-1282.

1210 Delgado-Cerezo, M., Sánchez-Rodríguez, C., Escudero, V., Miedes, E., Fernández, P.V., Jordá,
1211 L., Hernández-Blanco, C., Sánchez-Vallet, A., Bednarek, P., Schulze-Lefert, P., *et al.* (2012).
1212 Arabidopsis heterotrimeric G-protein regulates cell wall defense and resistance to necrotrophic
1213 fungi. Molecular Plant *5*, 98-114.
1214
1215 DeWire, S.M., Yamashita, D.S., Rominger, D.H., Liu, G., Cowan, C.L., Graczyk, T.M., Chen, X.-
1216 T., Pitis, P.M., Gotchev, D., Yuan, C., *et al.* (2013). A G protein-biased ligand at the μ-opioid
1217 receptor is potently analgesic with reduced gastrointestinal and respiratory dysfunction compared
1218 with morphine. Journal of Pharmacology and Experimental Therapeutics *344*, 708-717.
1219
1220 Dhonukshe, P., Aniento, F., Hwang, I., Robinson, D.G., Mravec, J., Stierhof, Y.-D., and Friml, J.
1221 (2007). Clathrin-mediated constitutive endocytosis of PIN auxin efflux carriers in Arabidopsis.
1222 Current Biology *17*, 520-527.
1223
1224 Ding, L., Pandey, S., and Assmann, S.M. (2008). Arabidopsis extra-large G proteins (XLGs)
1225 regulate root morphogenesis. The Plant Journal *53*, 248-263.
1226
1227 Droillard, M.-J., Boudsocq, M., Barbier-Brygoo, H., and Lauriere, C. (2004). Involvement of
1228 MPK4 in osmotic stress response pathways in cell suspensions and plantlets of *Arabidopsis*
1229 *thaliana*: activation by hypoosmolarity and negative role in hyperosmolarity tolerance. FEBS
1230 Letters *574*, 42-48.
1231
1232 Eichel, K., and von Zastrow, M. (2018). Subcellular organization of GPCR signaling. Trends in
1233 Pharmacological Sciences *39*, 200-208.
1234
1235 Escudero, V., Jordá, L., Sopeña-Torres, S., Mélida, H., Miedes, E., Muñoz-Barrios, A., Swami, S.,
1236 Alexander, D., McKee, L.S., Sánchez-Vallet, A., *et al.* (2017). Alteration of cell wall xylan
1237 acetylation triggers defense responses that counterbalance the immune deficiencies of plants
1238 impaired in the β-subunit of the heterotrimeric G-protein. The Plant Journal *92*, 386-399.
1239
1240 Fan, L., Li, R., Pan, J., Ding, Z., and Lin, J. (2015). Endocytosis and its regulation in plants. Trends
1241 in Plant Science *20*, 388-397.
1242
1243 Felix, G., Duran, J.D., Volko, S., and Boller, T. (1999). Plants have a sensitive perception system
1244 for the most conserved domain of bacterial flagellin. The Plant Journal *18*, 265-276.
1245
1246 Ferguson, K.M., Higashijima, T., Smigel, M.D., and Gilman, A.G. (1986). The influence of bound
1247 GDP on the kinetics of guanine nucleotide binding to G proteins. J Biol Chem *261*, 7393-7399.
1248
1249 Fernie, A.R., Roessner, U., and Geigenberger, P. (2001). The sucrose analog palatinose leads to a
1250 stimulation of sucrose degradation and starch synthesis when supplied to discs of growing potato
1251 tubers. Plant Physiol *125*, 1967-1977.
1252
1253 Fu, Y., Lim, S., Urano, D., Tunc-Ozdemir, M., Phan, N., Elston, T., and Jones, A. (2014).
1254 Reciprocal encoding of signal intensity and duration in a glucose-sensing circuit. . Cell *156*, 1084-
1255 1096.

Géhin, M., Vivat, V., Wurtz, J.-M., Losson, R., Chambon, P., Moras, D., and Gronemeyer, H. (1999). Structural basis for engineering of retinoic acid receptor isotype-selective agonists and antagonists. Chemistry & Biology *6*, 519-529.

Gesty-Palmer, D., Chen, M., Reiter, E., Ahn, S., Nelson, C.D., Wang, S., Eckhardt, A.E., Cowan, C.L., Spurney, R.F., Luttrell, L.M., *et al.* (2006). Distinct β-arrestin- and G protein-dependent pathways for parathyroid hormone receptor-stimulated ERK1/2 activation. Journal of Biological Chemistry *281*, 10856-10864.

Gómez-Gómez, L., and Boller, T. (2000). FLS2: An LRR receptor–like kinase involved in the perception of the bacterial elicitor flagellin in Arabidopsis. Molecular Cell *5*, 1003-1011.

Grigston, J.C., Osuna, D., Scheible, W.R., Stitt, M., and Jones, A.M. (2008). D-glucose sensing by a plasma membrane regulator of G signaling protein, AtRGS1. . FEBS Lett *582*, 3577-3584.

Gurevich, E., and Gurevich, V. (2006). Arrestins: ubiquitous regulators of cellular signaling pathways. Genome Biol *7*, 236.

Hao, H., Fan, L., Chen, T., Li, R., Li, X., He, Q., Botella, M.A., and Lin, J. (2014). Clathrin and membrane microdomains cooperatively regulate RbohD dynamics and activity in *Arabidopsis*. The Plant Cell *26*, 1729-1745.

Hirsch, J., Schubert, C., Gurevich, V., and Sigler, P. (1999). The 2.8 A crystal structure of visual arrestin: a model for arrestin's regulation. Cell *97*, 257 - 269.

Huot, B., Yao, J., Montgomery, B.L., and He, S.Y. (2014). Growth–defense tradeoffs in plants: A balancing act to optimize fitness. Molecular Plant *7*, 1267-1287.

Ilangumaran, S., and Hoessli, D.C. (1998). Effects of cholesterol depletion by cyclodextrin on the sphingolipid microdomains of the plasma membrane. Biochemical Journal *335*, 433-440.

Irani, N.G., Di Rubbo, S., Mylle, E., Van den Begin, J., Schneider-Pizoń, J., Hniliková, J., Šíša, M., Buyst, D., Vilarrasa-Blasi, J., Szatmári, A.-M., *et al.* (2012). Fluorescent castasterone reveals BRI1 signaling from the plasma membrane. Nature chemical biology *8*, 583.

Jackson, L.P., Kelly, B.T., McCoy, A.J., Gaffry, T., James, L.C., Collins, B.M., Höning, S., Evans, P.R., and Owen, D.J. (2010). A large-scale conformational change couples membrane recruitment to cargo binding in the AP2 clathrin adaptor Complex. Cell *141*, 1220-1229.

Jelenska, J., Davern, S.M., Standaert, R.F., Mirzadeh, S., and Greenberg, J.T. (2017). Flagellin peptide flg22 gains access to long-distance trafficking in Arabidopsis via its receptor, FLS2. Journal of Experimental Botany *68*, 1769-1783.

Jha, S.G., Larson, E.R., Humble, J., Domozych, D.S., Barrington, D.S., and Tierney, M.L. (2018). Vacuolar Protein Sorting 26C encodes an evolutionarily conserved large retromer subunit in

eukaryotes that is important for root hair growth in Arabidopsis thaliana. The Plant Journal *94*, 595-611.

Johnston, C.A., Taylor, J.P., Gao, Y., Kimple, A.J., Grigston, J.C., Chen, J.-G., Siderovski, D.P., Jones, A.M., and Willard, F.S. (2007). GTPase acceleration as the rate-limiting step in Arabidopsis G protein-coupled sugar signaling. Proceedings of the National Academy of Sciences *104*, 17317-17322.

Jones, J., Duffy, J., M, M., Temple, B., Dohlman, H., and Jones, A. (2011a). The crystal structure of a self-activating G protein α subunit reveals its distinct mechanism of signal initiation. Sci Signal *4*, ra8.

Jones, J.C., Temple, B.R.S., Jones, A.M., and Dohlman, H.G. (2011b). Functional reconstitution of an atypical G protein heterotrimer and regulator of G protein signaling protein (RGS1) from *Arabidopsis thaliana*. Journal of Biological Chemistry *286*, 13143-13150.

Kalderon, D., Roberts, B.L., Richardson, W.D., and Smith, A.E. (1984). A short amino acid sequence able to specify nuclear location. Cell *39*, 499-509.

Kang, Y., Zhou, X.E., Gao, X., He, Y., Liu, W., Ishchenko, A., Barty, A., White, T.A., Yefanov, O., Han, G.W.*, et al.* (2015). Crystal structure of rhodopsin bound to arrestin by femtosecond X-ray laser. Nature *523*, 561.

Keinath, N.F., Waadt, R., Brugman, R., Schroeder, Julian I., Grossmann, G., Schumacher, K., and Krebs, M. (2015). Live cell imaging with R-GECO1 sheds light on flg22- and chitin-induced transient $[Ca^{2+}]_{cyt}$ patterns in Arabidopsis. Molecular Plant *8*, 1188-1200.

Kelly, B.T., McCoy, A.J., Späte, K., Miller, S.E., Evans, P.R., Höning, S., and Owen, D.J. (2008). A structural explanation for the binding of endocytic dileucine motifs by the AP2 complex. Nature *456*, 976.

Kim, M., Vishnivetskiy, S.A., Van Eps, N., Alexander, N.S., Cleghorn, W.M., Zhan, X., Hanson, S.M., Morizumi, T., Ernst, O.P., Meiler, J.*, et al.* (2012). Conformation of receptor-bound visual arrestin. Proceedings of the National Academy of Sciences *109*, 18407-18412.

Kim, S.Y., Xu, Z.-Y., Song, K., Kim, D.H., Kang, H., Reichardt, I., Sohn, E.J., Friml, J., Juergens, G., and Hwang, I. (2013). Adaptor protein complex 2–mediated endocytosis is crucial for male reproductive organ development in *Arabidopsis*. The Plant Cell *25*, 2970-2985.

Klopffleisch, K., Phan, N., Augustin, K., Bayne, R.S., Booker, K.S., Botella, J.R., Carpita, N.C., Carr, T., Chen, J.-G., Cooke, T.R.*, et al.* (2011). Arabidopsis G-protein interactome reveals connections to cell wall carbohydrates and morphogenesis. Mol Syst Biol *7*, 532.

Krauss, M., Kukhtina, V., Pechstein, A., and Haucke, V. (2006). Stimulation of phosphatidylinositol kinase type I-mediated phosphatidylinositol (4,5)-bisphosphate synthesis by AP-2μ–cargo complexes. Proceedings of the National Academy of Sciences *103*, 11934-11939.

Lee, J., Eschen-Lippold, L., Lassowskat, I., Böttcher, C., and Scheel, D. (2015). Cellular reprogramming through mitogen-activated protein kinases. Frontiers in Plant Science *6*.

Li, L., and Sheen, J. (2016). Dynamic and diverse sugar signaling. Current Opinion in Plant Biology *33*, 116-125.

Li, R., Liu, P., Wan, Y., Chen, T., Wang, Q., Mettbach, U., Baluška, F., Šamaj, J., Fang, X., Lucas, W.J., *et al.* (2012). A membrane microdomain-associated protein, Arabidopsis Flot1, is involved in a clathrin-independent endocytic pathway and is required for seedling development. The Plant Cell *24*, 2105-2122.

Li, X., Wang, X., Yang, Y., Li, R., He, Q., Fang, X., Luu, D.-T., Maurel, C., and Lin, J. (2011). Single-molecule analysis of PIP2;1 dynamics and partitioning reveals multiple modes of Arabidopsis plasma membrane aquaporin regulation. The Plant Cell *23*, 3780-3797.

Liang, X., Ma, M., Zhou, Z., Wang, J., Yang, X., Rao, S., Bi, G., Li, L., Zhang, X., Chai, J., *et al.* (2018). Ligand-triggered de-repression of Arabidopsis heterotrimeric G proteins coupled to immune receptor kinases. Cell Research.

Liao, K.-L., Melvin, C.E., Sozzani, R., Jones, R.D., Elston, T.C., and Jones, A.M. (2017). Dose-Duration Reciprocity for G protein activation: Modulation of kinase to substrate ratio alters cell signaling. PLoS ONE *12*, e0190000.

Lin, W.-W., and Hsieh, S.-L. (2011). Decoy receptor 3: A pleiotropic immunomodulator and biomarker for inflammatory diseases, autoimmune diseases and cancer. Biochemical Pharmacology *81*, 838-847.

Lin, Z.-J.D., Liebrand, T.W.H., Yadeta, K.A., and Coaker, G. (2015). PBL13 is a serine/threonine protein kinase that negatively regulates Arabidopsis immune responses. Plant Physiology *169*, 2950-2962.

Lohse, M., Benovic, J., Codina, J., Caron, M., and Lefkowitz, R. (1990). beta-Arrestin: a protein that regulates beta-adrenergic receptor function. Science *248*, 1547 - 1550.

Loreti, E., Alpi, A., and Perata, P. (2000). Glucose and disaccharide-sensing mechanisms modulate the expression of alpha -amylase in barley embryos. Plant Physiol *123*, 939-948.

Luttrell, L.M., Roudabush, F.L., Choy, E.W., Miller, W.E., Field, M.E., Pierce, K.L., and Lefkowitz, R.J. (2001). Activation and targeting of extracellular signal-regulated kinases by β-arrestin scaffolds. Proceedings of the National Academy of Sciences *98*, 2449-2454.

Manglik, A., Lin, H., Aryal, D.K., McCorvy, J.D., Dengler, D., Corder, G., Levit, A., Kling, R.C., Bernat, V., Hübner, H., *et al.* (2016). Structure-based discovery of opioid analgesics with reduced side effects. Nature *537*, 185.

1394 Martí-Renom, M.A., Stuart, A.C., Fiser, A., Sánchez, R., and, F.M., and Šali, A. (2000).
1395 Comparative protein structure modeling of genes and genomes. Annual Review of Biophysics and
1396 Biomolecular Structure *29*, 291-325.
1397
1398 Mudgil, Y., Karve, A., Teixeira, P., Jiang, K., Tunc-Ozdemir, M., and Jones, A. (2016).
1399 Photosynthate regulation of the root system architecture mediated by the heterotrimeric G protein
1400 complex in Arabidopsis. Frontiers in Plant Science *7*.
1401
1402 Nobles, K.N., Xiao, K., Ahn, S., Shukla, A.K., Lam, C.M., Rajagopal, S., Strachan, R.T., Huang,
1403 T.-Y., Bressler, E.A., Hara, M.R.*, et al.* (2011). Distinct phosphorylation sites on the β_2-adrenergic
1404 receptor establish a barcode that encodes differential functions of β-arrestin. Science Signaling *4*,
1405 ra51-ra51.
1406
1407 O'Hayre, M., Eichel, K., Avino, S., Zhao, X., Steffen, D.J., Feng, X., Kawakami, K., Aoki, J.,
1408 Messer, K., Sunahara, R.*, et al.* (2017). Genetic evidence that β-arrestins are dispensable for the
1409 initiation of β_2 adrenergic receptor signaling to ERK. Science Signaling *10*, eaal3395.
1410
1411 Ohno, H., Stewart, J., Fournier, M., Bosshart, H., Rhee, I., Miyatake, S., Saito, T., Gallusser, A.,
1412 Kirchhausen, T., and Bonifacino, J. (1995). Interaction of tyrosine-based sorting signals with
1413 clathrin-associated proteins. Science *269*, 1872-1875.
1414
1415 Ohtani, Y., Irie, T., Uekama, K., Fukunaga, K., and Pitha, J. (1989). Differential effects of alpha-
1416 , beta- and gamma-cyclodextrins on human erythrocytes. Eur J Biochem *186*, 17-22.
1417
1418 Oliviusson, P., Heinzerling, O., Hillmer, S., Hinz, G., Tse, Y.C., Jiang, L., and Robinson, D.G.
1419 (2006). Plant retromer, Localized to the prevacuolar compartment and microvesicles in
1420 *Arabidopsis*, may interact with vacuolar sorting receptors. The Plant Cell *18*, 1239-1252.
1421
1422 Paing, M.M., Stutts, A.B., Kohout, T.A., Lefkowitz, R.J., and Trejo, J. (2002). β-arrestins regulate
1423 protease-activated receptor-1 desensitization but not internalization or down-regulation. Journal of
1424 Biological Chemistry *277*, 1292-1300.
1425
1426 Pan, G., Ni, J., Wei, Y.-F., Yu, G.-l., Gentz, R., and Dixit, V.M. (1997). An antagonist decoy
1427 receptor and a death domain-containing receptor for TRAIL. Science *277*, 815-818.
1428
1429 Patwari, P., and Lee, R.T. (2012). An expanded family of arrestins regulate metabolism. Trends in
1430 Endocrinology & Metabolism *23*, 216-222.
1431 Peterson, Y.K., and Luttrell, L.M. (2017). The diverse roles of arrestin scaffolds in G protein–
1432 coupled receptor signaling. Pharmacological Reviews *69*, 256-297.
1433
1434 Pharr, D., and Keller, F. (2017). In Photoassimilate distribution plants and crops sSource-sink
1435 relationships (Routledge), pp. 157-183.
1436
1437 Raffaele, S., Bayer, E., Lafarge, D., Cluzet, S., German Retana, S., Boubekeur, T., Leborgne-
1438 Castel, N., Carde, J.-P., Lherminier, J., Noirot, E.*, et al.* (2009). Remorin, a solanaceae protein

resident in membrane rafts and plasmodesmata, impairs potato virus X movement. The Plant Cell *21*, 1541-1555.

Rajagopal, S., Kim, J., Ahn, S., Craig, S., Lam, C.M., Gerard, N.P., Gerard, C., and Lefkowitz, R.J. (2010a). β-arrestin- but not G protein-mediated signaling by the "decoy" receptor CXCR7. Proceedings of the National Academy of Sciences *107*, 628-632.

Rajagopal, S., Rajagopal, K., and Lefkowitz, R.J. (2010b). Teaching old receptors new tricks: biasing seven-transmembrane receptors. Nature Reviews Drug Discovery *9*, 373.

Ranf, S., Eschen-Lippold, L., Pecher, P., Lee, J., and Scheel, D. (2011). Interplay between calcium signalling and early signalling elements during defence responses to microbe- or damage-associated molecular patterns. The Plant Journal *68*, 100-113.

Rives, M.-L., Rossillo, M., Liu-Chen, L.-Y., and Javitch, J.A. (2012). 6′-Guanidinonaltrindole (6′-GNTI) is a G protein-biased κ-opioid receptor agonist that inhibits arrestin recruitment. Journal of Biological Chemistry *287*, 27050-27054.

Rolland, F., Moore, B., and Sheen, J. (2002). Sugar sensing and signaling in plants. The Plant Cell *14*, S185-S205.

Schindelin, J., Arganda-Carreras, I., Frise, E., Kaynig, V., Longair, M., Pietzsch, T., Preibisch, S., Rueden, C., Saalfeld, S., Schmid, B.*, et al.* (2012). Fiji: an open-source platform for biological-image analysis. Nature Methods *9*, 676.

Shenoy, S.K., Drake, M.T., Nelson, C.D., Houtz, D.A., Xiao, K., Madabushi, S., Reiter, E., Premont, R.T., Lichtarge, O., and Lefkowitz, R.J. (2006). β-Arrestin-dependent, G protein-independent ERK1/2 activation by the β2 adrenergic receptor. Journal of Biological Chemistry *281*, 1261-1273.

Shi, H., Rojas, R., Bonifacino, J.S., and Hurley, J.H. (2006). The retromer subunit Vps26 has an arrestin fold and binds Vps35 through its C-terminal domain. Nature Structural & Molecular Biology *13*, 540-548.

Shiraishi, Y., Natsume, M., Kofuku, Y., Imai, S., Nakata, K., Mizukoshi, T., Ueda, T., Iwaï, H., and Shimada, I. (2018). Phosphorylation-induced conformation of β2-adrenoceptor related to arrestin recruitment revealed by NMR. Nature Communications *9*, 194.

Shiu, S.H., and Bleecker, A.B. (2001). Plant receptor-llike gene family: diversity, function, and signaling. Science STKE *Dec. 18th*, RE22.

Shukla, A.K., Manglik, A., Kruse, A.C., Xiao, K., Reis, R.I., Tseng, W.-C., Staus, D.P., Hilger, D., Uysal, S., Huang, L.-Y.*, et al.* (2013). Structure of active β-arrestin-1 bound to a G-protein-coupled receptor phosphopeptide. Nature *497*, 137.

Sibley, D.R., Benovic, J.L., Caron, M.G., and Lefkowitz, R.J. (1987). Regulation of transmembrane signaling by receptor phosphorylation. Cell *48*, 913-922.

Sinha, A.K., Hofmann, M.G., Romer, U., Kockenberger, W., Elling, L., and Roitsch, T. (2002). Metabolizable and non-metabolizable sugars activate different signal transduction pathways in tomato. Plant Physiol *128*, 1480-1489.

Smith, J.S., Lefkowitz, R.J., and Rajagopal, S. (2018). Biased signalling: from simple switches to allosteric microprocessors. Nature Reviews Drug Discovery *17*, 243.

Smith, T.H., Coronel, L.J., Li, J.G., Dores, M.R., Nieman, M.T., and Trejo, J. (2016). Protease-activated receptor-4 signaling and trafficking is regulated by the clathrin adaptor protein complex-2 independent of β-arrestins. Journal of Biological Chemistry *291*, 18453-18464.

Sun, Y., Li, L., Macho, A.P., Han, Z., Hu, Z., Zipfel, C., Zhou, J.-M., and Chai, J. (2013). Structural basis for flg22-induced activation of the *Arabidopsis* FLS2-BAK1 immune complex. Science *342*, 624-628.

Tunc-Ozdemir, M., and Jones, A.M. (2017). Ligand-induced dynamics of heterotrimeric G protein-coupled receptor-like kinase complexes. PLoS ONE *12*, e0171854.

Tunc-Ozdemir, M., Li, B., Jaiswal, D.K., Urano, D., Jones, A.M., and Torres, M.P. (2017). Predicted functional implications of phosphorylation of regulator of G protein signaling protein in plants. Frontiers in Plant Science *8*.

Tunc-Ozdemir, M., Liao, K.-L., Ross-Elliott, T.J., Elston, T.C., and Jones, A.M. (2018). Long-distance communication in Arabidopsis involving a self-activating G protein. Plant Direct *2*, e00037.

Tunc-Ozdemir, M., Urano, D., Jaiswal, D.K., Clouse, S.D., and Jones, A.M. (2016). Direct modulation of heterotrimeric G protein-coupled signaling by a receptor kinase complex. Journal of Biological Chemistry *291*, 13918-13925.

Urano, D., Maruta, N., Trusov, Y., Stoian, R., Liang, Y., Jaiswal, D., Thung, L., Botella, J., and Jones, A. (2016). Saltatory evolution of the heterotrimeric G protein signaling mechanisms in the plant kingdom. Science Signaling *9*, ra93.

Urano, D., Phan, N., Jones, J.C., Yang, J., Huang, J., Grigston, J., Philip Taylor, J., and Jones, A.M. (2012). Endocytosis of the seven-transmembrane RGS1 protein activates G-protein-coupled signalling in Arabidopsis. Nat Cell Biol *14*, 1079-1088.

Urs, N.M., Gee, S.M., Pack, T.F., McCorvy, J.D., Evron, T., Snyder, J.C., Yang, X., Rodriguiz, R.M., Borrelli, E., Wetsel, W.C.*, et al.* (2016). Distinct cortical and striatal actions of a β-arrestin–biased dopamine D2 receptor ligand reveal unique antipsychotic-like properties. Proceedings of the National Academy of Sciences *113*, E8178-E8186.

Urs, N.M., Peterson, S.M., and Caron, M.G. (2017). New concepts in dopamine D2 receptor biased signaling and implications for schizophrenia therapy. Biological Psychiatry *81*, 78-85.

Vang, S., Seitz, K., and Krysan, P. (2018). A simple microfluidic device for live cell imaging of Arabidopsis cotyledons, leaves, and seedlings. Biotechniques *64*, 255-261.

Vishnivetskiy, S.A., Gimenez, L.E., Francis, D.J., Hanson, S.M., Hubbell, W.L., Klug, C.S., and Gurevich, V.V. (2011). Few residues within an extensive binding interface drive receptor interaction and determine the specificity of arrestin proteins. Journal of Biological Chemistry *286*, 24288-24299.

Vishnivetskiy, S.A., Paz, C.L., Schubert, C., Hirsch, J.A., Sigler, P.B., and Gurevich, V.V. (1999). How does arrestin respond to the phosphorylated state of rhodopsin? Journal of Biological Chemistry *274*, 11451-11454.

Wagemans, J., and Lavigne, R. (2015). Identification of protein-protein interactions by standard Gal4p-based yeast two-hybrid screening. In Protein-Protein Interactions: Methods and Applications, C.L. Meyerkord, and H. Fu, eds. (New York, NY, Springer New York), pp. 409-431.

Wen, W., Meinkotht, J.L., Tsien, R.Y., and Taylor, S.S. (1995). Identification of a signal for rapid export of proteins from the nucleus. Cell *82*, 463-473.

White, K.L., Robinson, J.E., Zhu, H., DiBerto, J.F., Polepally, P.R., Zjawiony, J.K., Nichols, D.E., Malanga, C.J., and Roth, B.L. (2015). The G protein–biased opioid receptor agonist RB-64 is analgesic with a unique spectrum of activities *in vivo*. Journal of Pharmacology and Experimental Therapeutics *352*, 98-109.

Williams, L.E., Lemoine, R., and Sauer, N. (2000). Sugar transporters in higher plants – a diversity of roles and complex regulation. Trends in Plant Science *5*, 283-290.

Wingler, L.M., Elgeti, M., Hilger, D., Latorraca, N.R., Lerch, M.T., Staus, D.P., Dror, R.O., Kobilka, B.K., Hubbell, W.L., and Lefkowitz, R.J. (2019). Angiotensin analogs with divergent bias stabilize distinct receptor conformations. Cell *176*, 468-478.e411.

Wu, L., and Birch, R. (2011). Isomaltulose is actively metabolized in plant cells. Plant Physiol *157*, 2094-2101.

Yang, F., Yu, X., Liu, C., Qu, C.-X., Gong, Z., Liu, H.-D., Li, F.-H., Wang, H.-M., He, D.-F., Yi, F.*, et al.* (2015). Phospho-selective mechanisms of arrestin conformations and functions revealed by unnatural amino acid incorporation and 19F-NMR. Nature Communications *6*, 8202.

Yang, Z., Yang, F., Zhang, D., Liu, Z., Lin, A., Liu, C., Xiao, P., Yu, X., and Sun, J.-P. (2017). Phosphorylation of G protein-coupled receptors: from the barcode hypothesis to the flute model. Molecular pharmacology *92*, 201-210.

Zaman, N., Seitz, K., Kabir, M., George-Schreder, L.S., Shepstone, I., Liu, Y., Zhang, S., and Krysan, P.J. (2019). A Förster resonance energy transfer sensor for live-cell imaging of mitogen-activated protein kinase activity in Arabidopsis. The Plant Journal *97*, 970-983.

Zelazny, E., Santambrogio, M., Pourcher, M., Chambrier, P., Berne-Dedieu, A., Fobis-Loisy, I., Miège, C., Jaillais, Y., and Gaude, T. (2013). Mechanisms governing the endosomal membrane recruitment of the core retromer in Arabidopsis. Journal of Biological Chemistry *288*, 8815-8825.

Zhan, X., Gimenez, L.E., Gurevich, V.V., and Spiller, B.W. (2011). Crystal structure of arrestin-3 reveals the basis of the difference in receptor binding between two non-visual subtypes. Journal of Molecular Biology *406*, 467-478.

Zhong, C.-L., Zhang, C., and Liu, J.-Z. (2018). Heterotrimeric G protein signaling in plant immunity. Journal of Experimental Botany *70*, 1109-1118.

Zhou, Z., Bi, G., and Zhou, J.-M. (2018). Luciferase complementation assay for protein-protein interactions in plants. Current Protocols in Plant Biology *3*, 42-50.

Figure 1

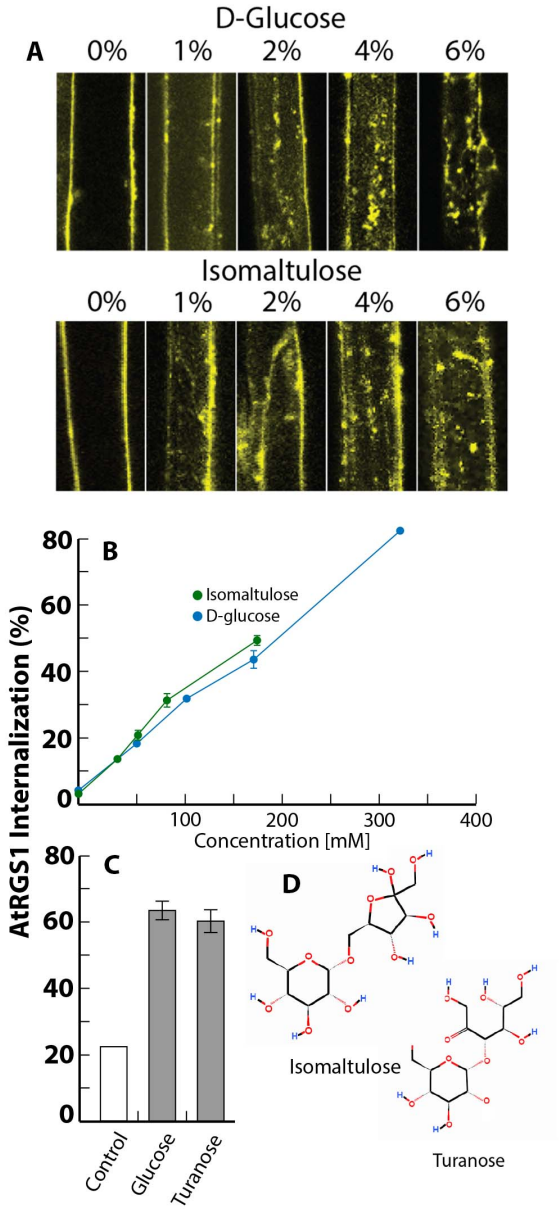

Figure 2

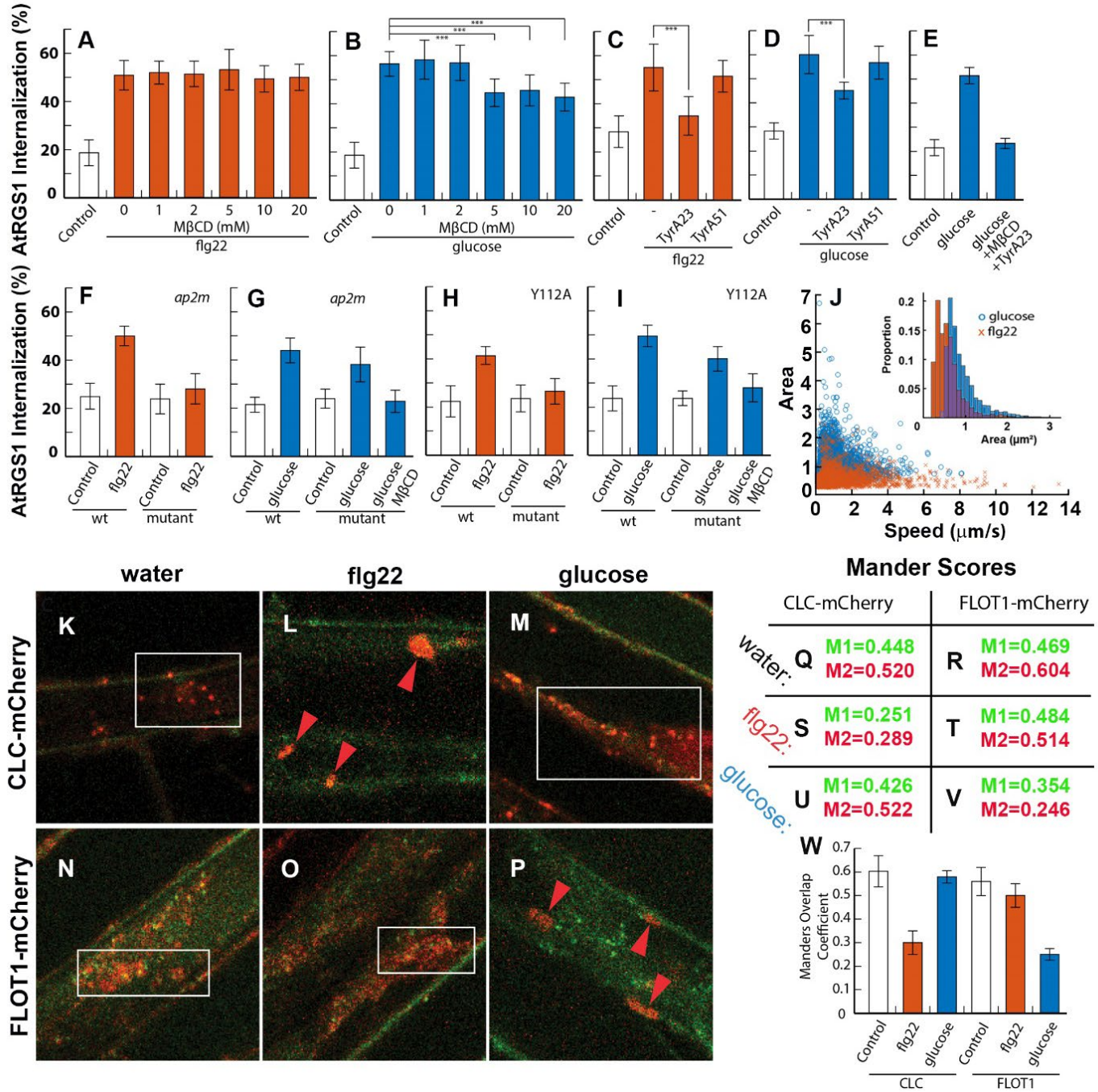

Figure 3

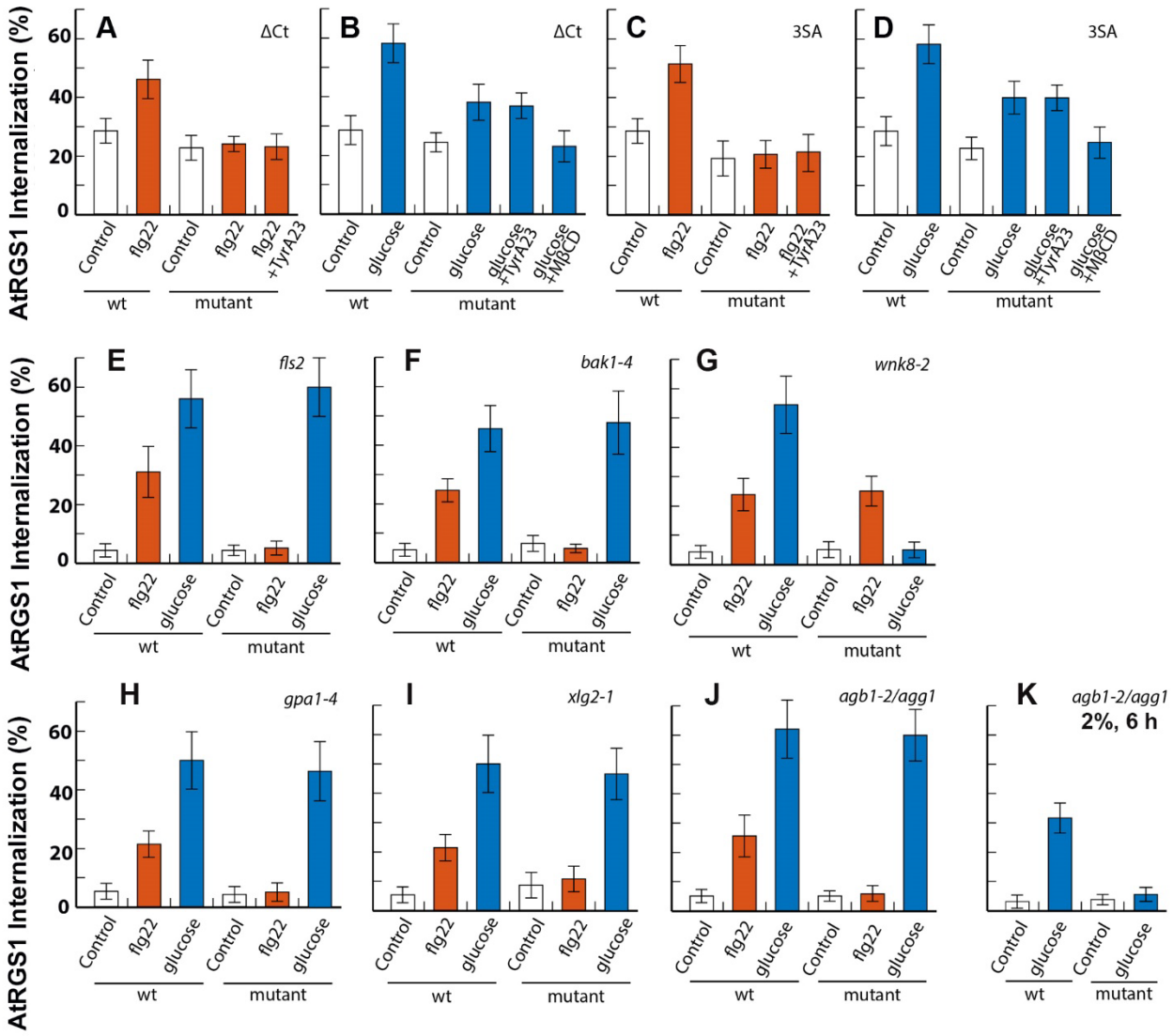

1643 Figure 4
1644

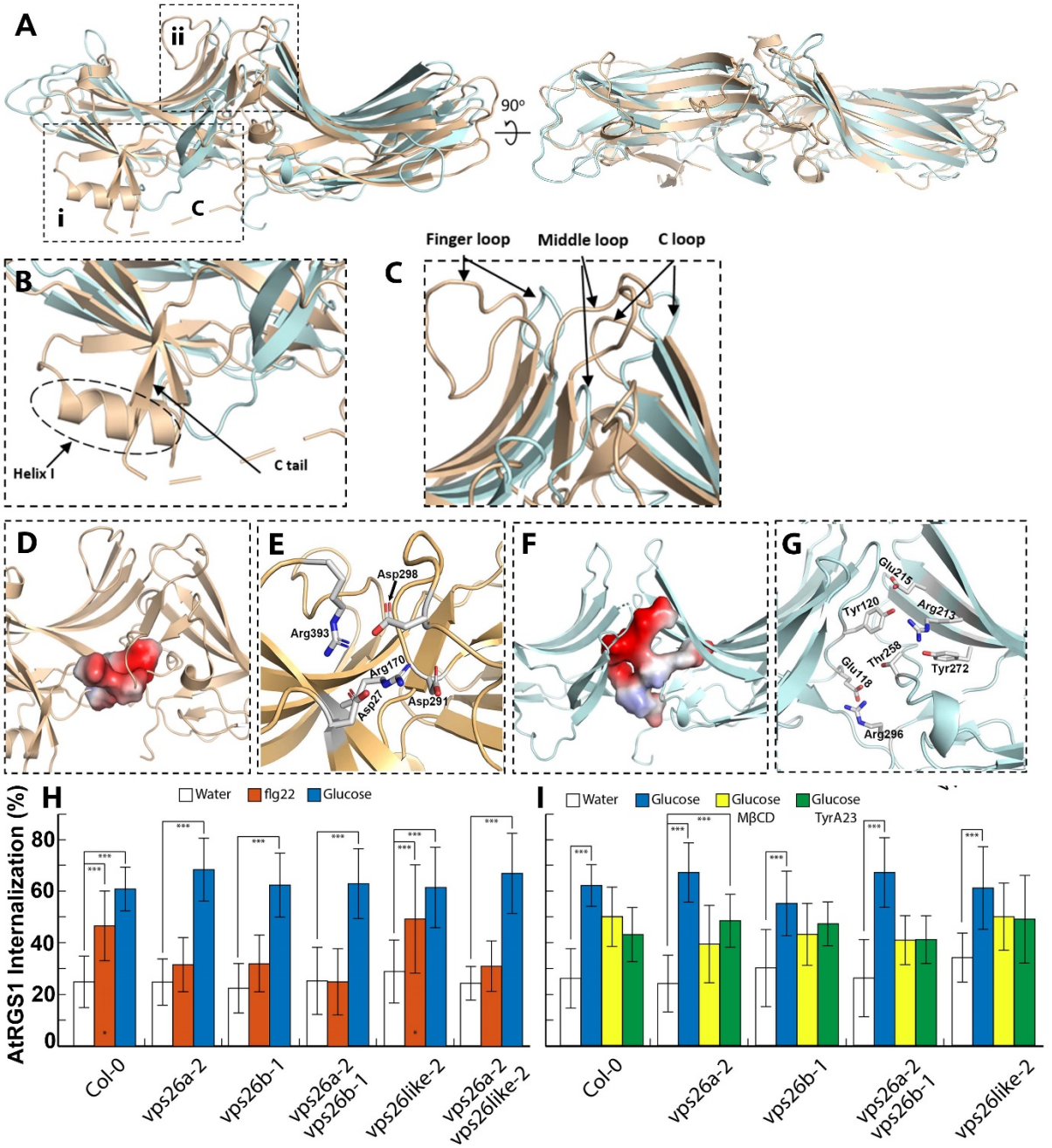

1645
1646
1647
1648
1649
1650
1651
1652

Figure 5

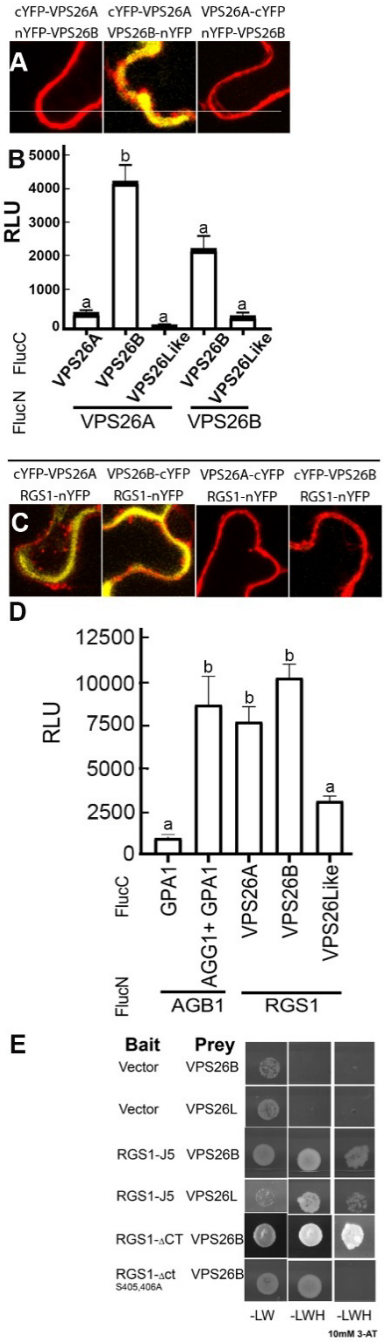

Figure 6

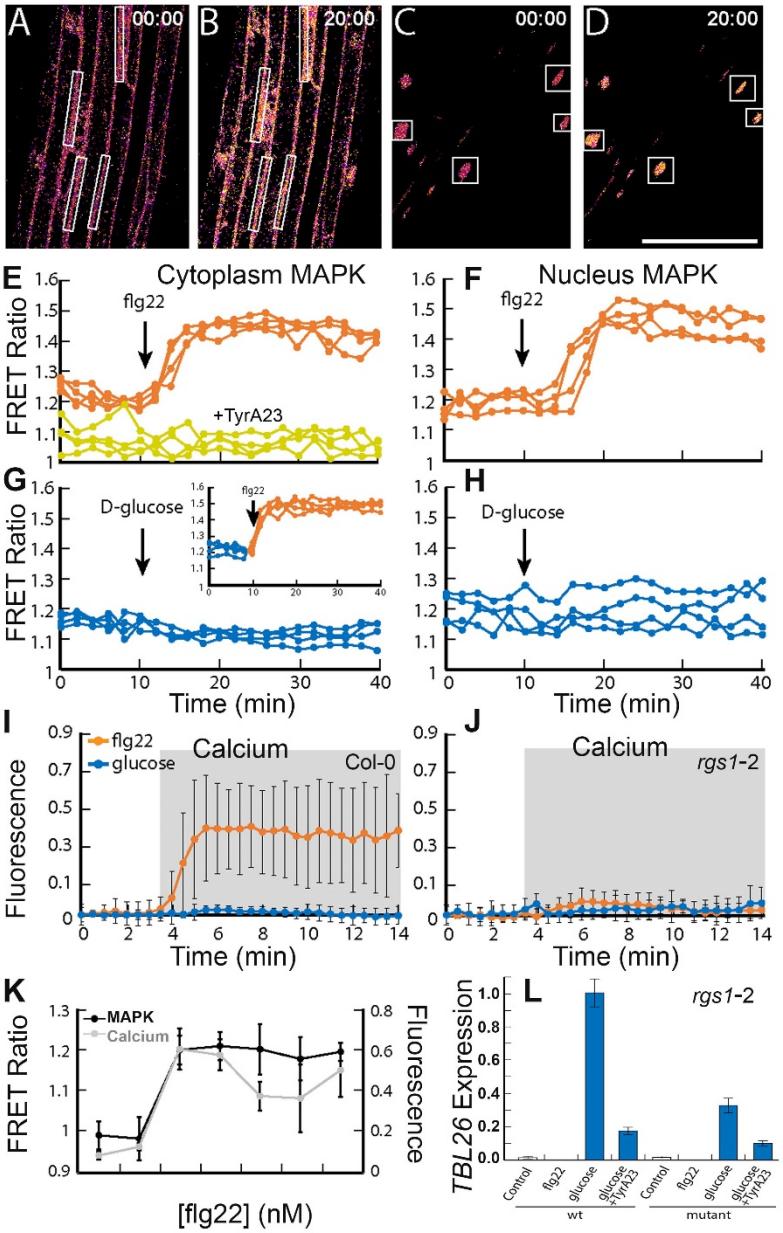

Figure 7

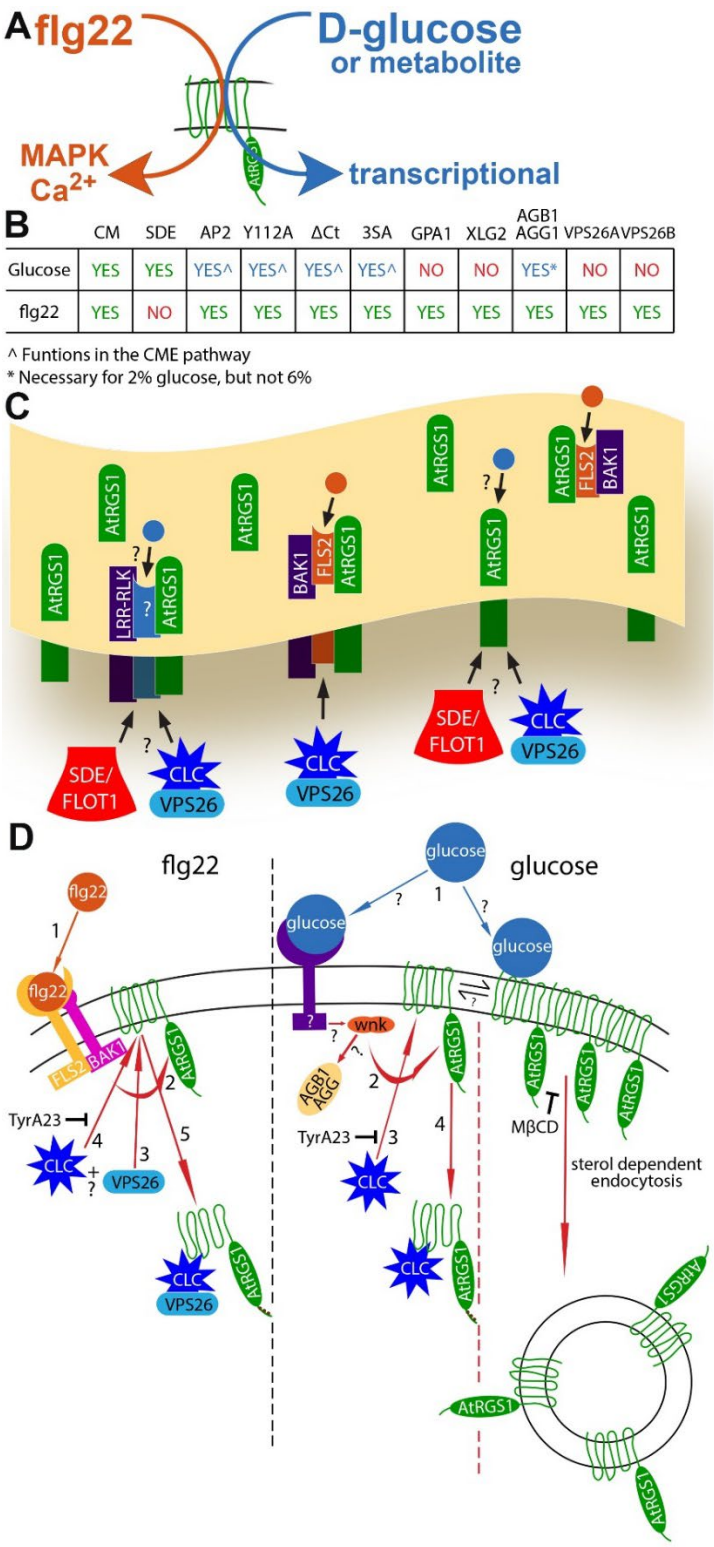

	CM	SDE	AP2	Y112A	ΔCt	3SA	GPA1	XLG2	AGB1 AGG1	VPS26A	VPS26B
Glucose	YES	YES	YES^	YES^	YES^	YES^	NO	NO	YES*	NO	NO
flg22	YES	NO	YES	YES	YES	YES	YES	YES	YES	YES	YES

^ Funtions in the CME pathway
* Necessary for 2% glucose, but not 6%

Figure S1

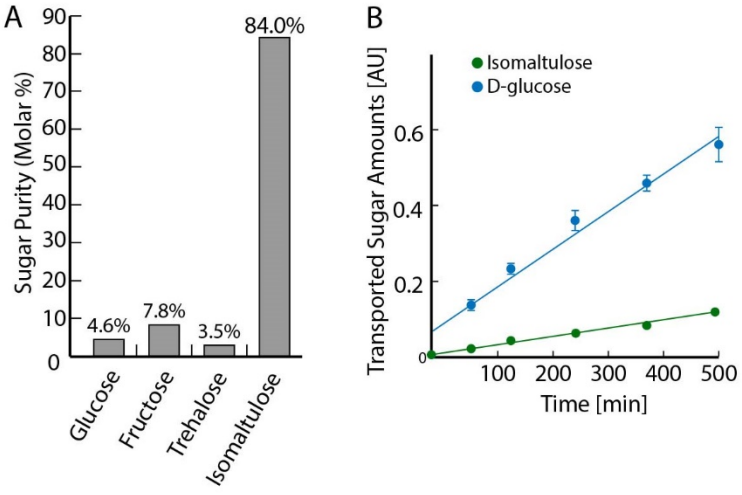

Figure S2

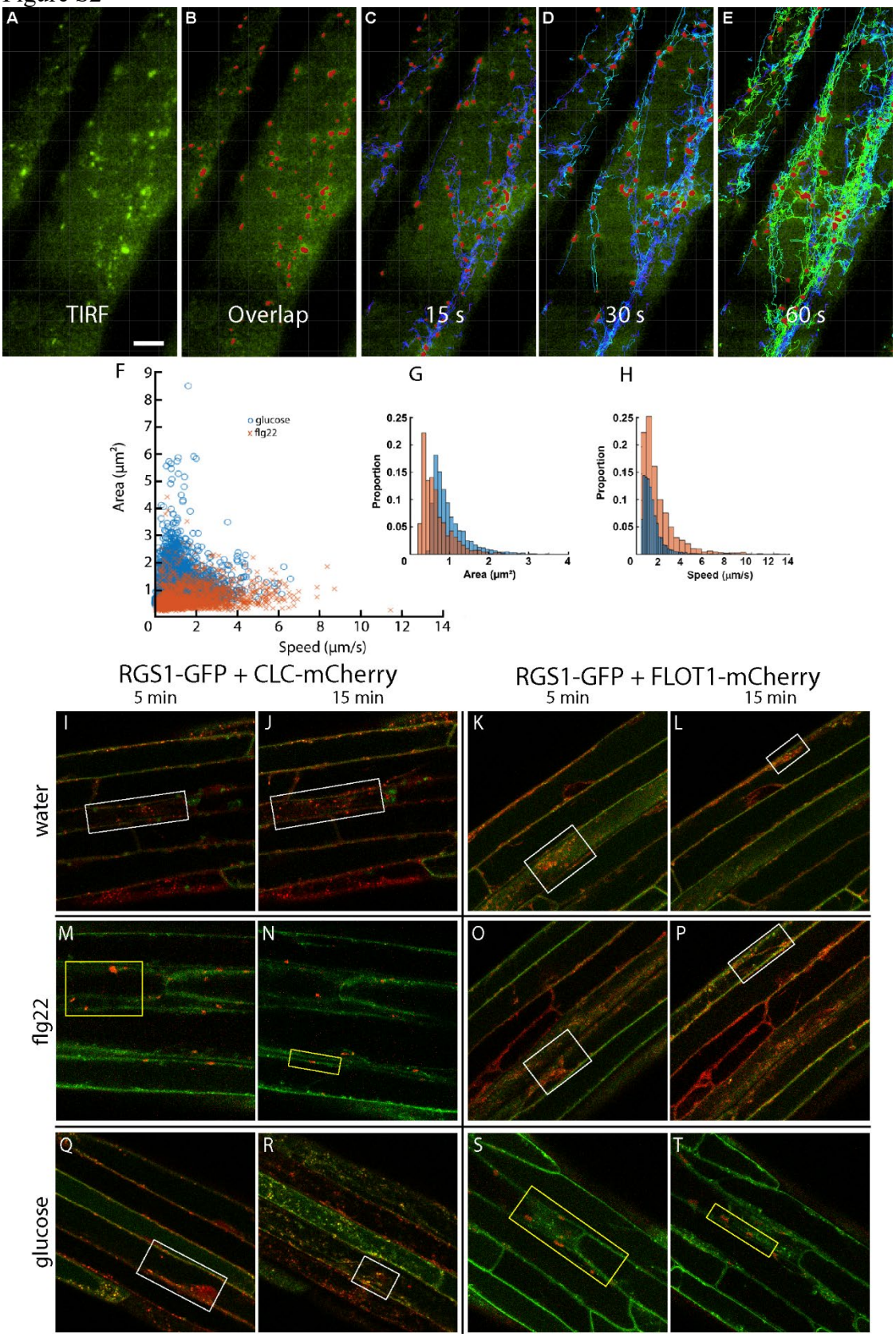

Figure S3

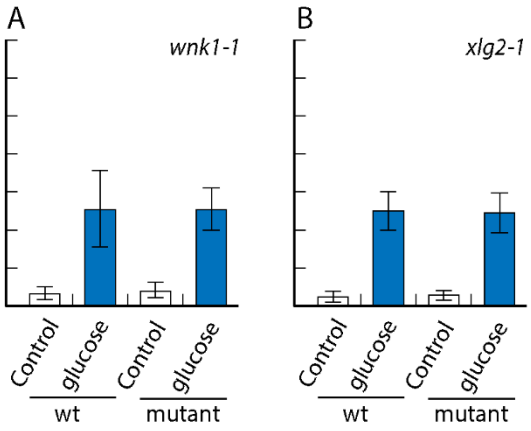

Figure S4

A

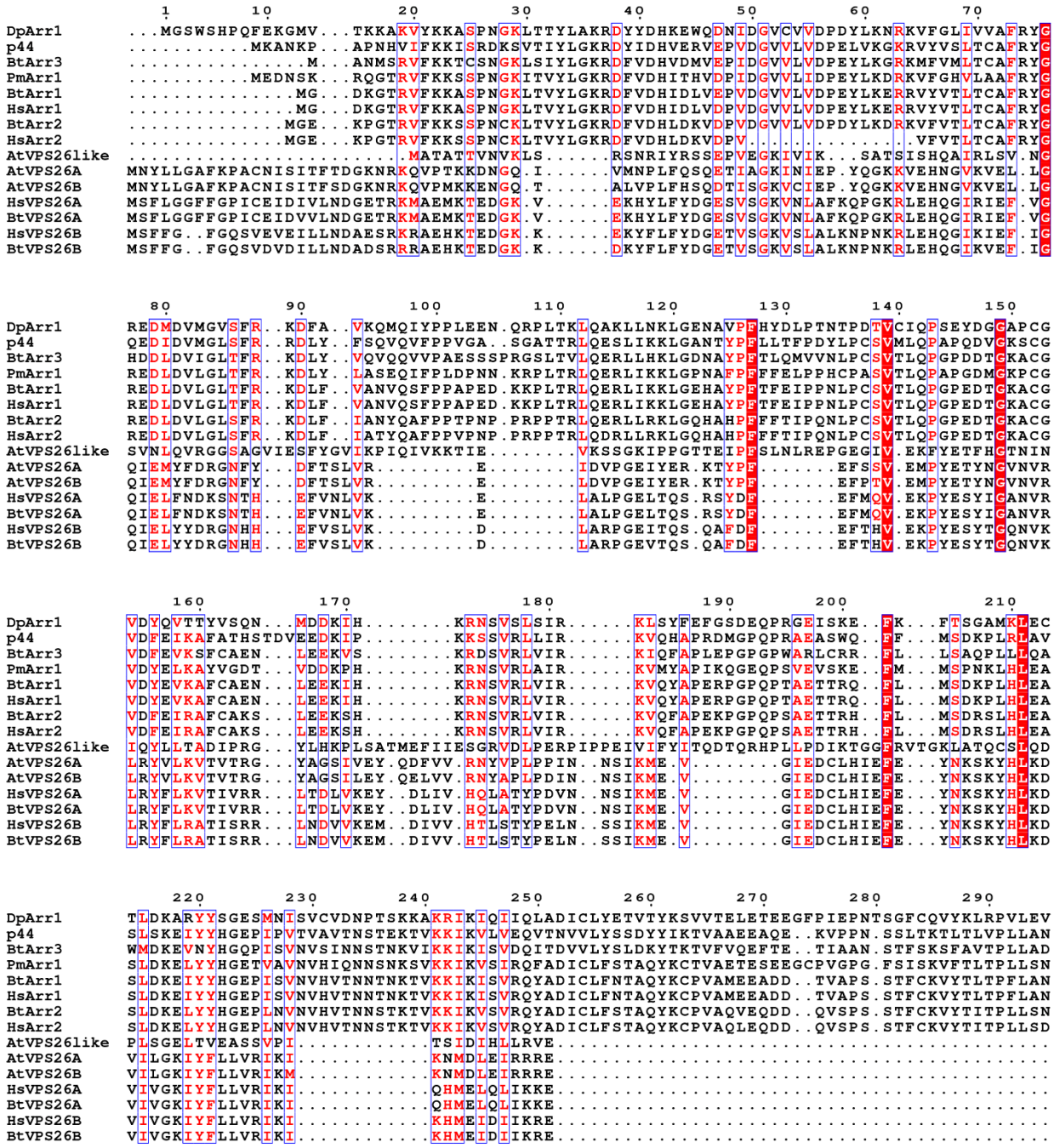

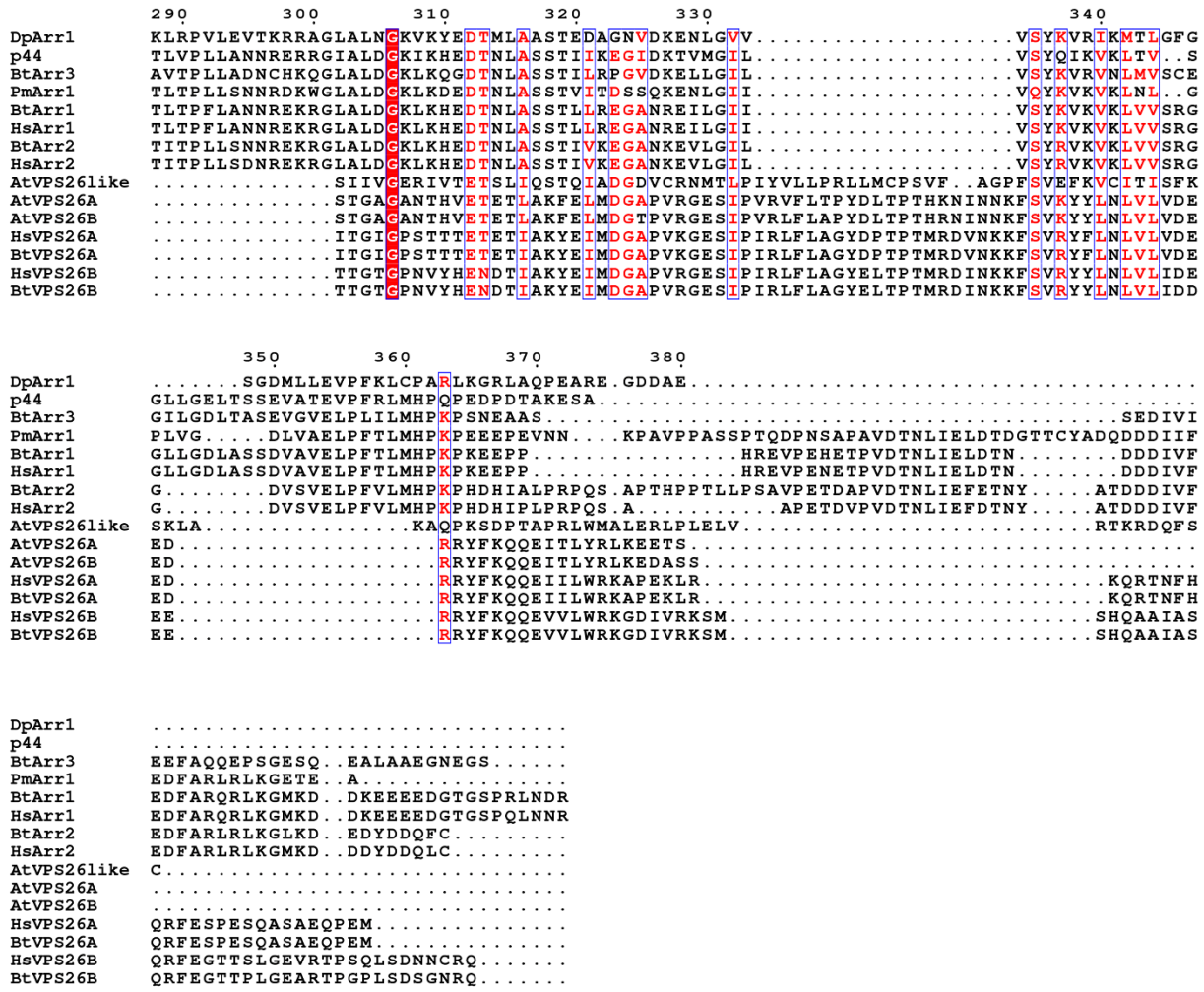

B.

1: DpArr1	100.00	37.22	38.42	46.98	46.61	46.89	43.13	42.03	19.03	18.22	19.77	15.44	15.44	16.73	16.73
2: p44		100.00	52.79	49.72	59.50	59.22	56.46	56.01	18.56	15.16	15.16	12.65	12.65	12.24	12.65
3: BtArr3			100.00	50.00	60.77	60.51	56.58	54.79	17.10	16.03	16.03	13.51	13.51	14.61	16.10
4: PmArr1				100.00	66.33	66.58	63.48	63.09	17.86	17.41	18.55	12.96	12.96	14.65	15.02
5: BtArr1					100.00	99.04	77.81	78.33	17.54	19.83	19.83	14.67	14.67	15.36	16.10
6: HsArr1						100.00	78.05	78.59	17.16	19.41	20.25	14.29	14.29	14.98	15.73
7: BtArr2							100.00	96.95	17.02	14.11	14.86	12.50	12.50	13.88	14.23
8: HsArr2								100.00	16.79	13.91	14.35	11.51	11.51	13.90	14.29
9: AtVPS26like									100.00	21.61	19.71	21.35	21.35	20.42	20.07
10: AtVPS26A										100.00	91.06	56.48	56.15	54.18	53.51
11: AtVPS26B											100.00	57.95	57.62	55.00	54.33
12: HsVPS26A												100.00	99.69	70.46	68.92
13: BtVPS26A													100.00	70.15	68.62
14: HsVPS26B														100.00	95.54
15: BtVPS26B															100.00

C.

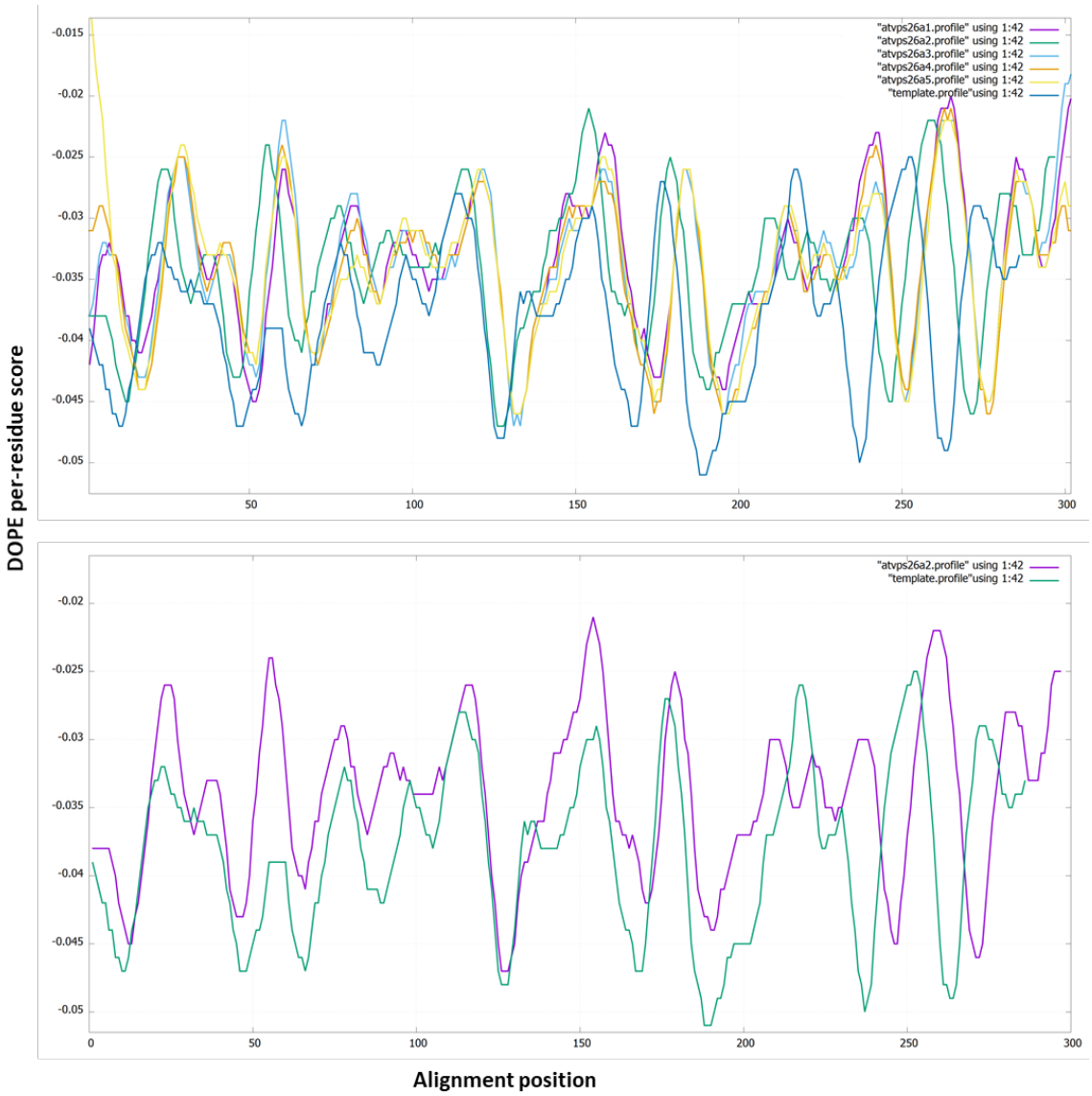

1768 D.

Filename	molpdf	DOPE score	GA341 score	RMSD
atvps26a1.pdb	2292.41699	-30278.39648	1.00000	0.309
atvps26a2.pdb	2233.81055	-30840.71289	1.00000	0.17
atvps26a3.pdb	2258.48999	-30400.76953	1.00000	0.277
atvps26a4.pdb	2212.42798	-30568.29883	1.00000	0.244
atvps26a5.pdb	2188.86987	-30466.78711	1.00000	0.217

1769

1770 E.

1771

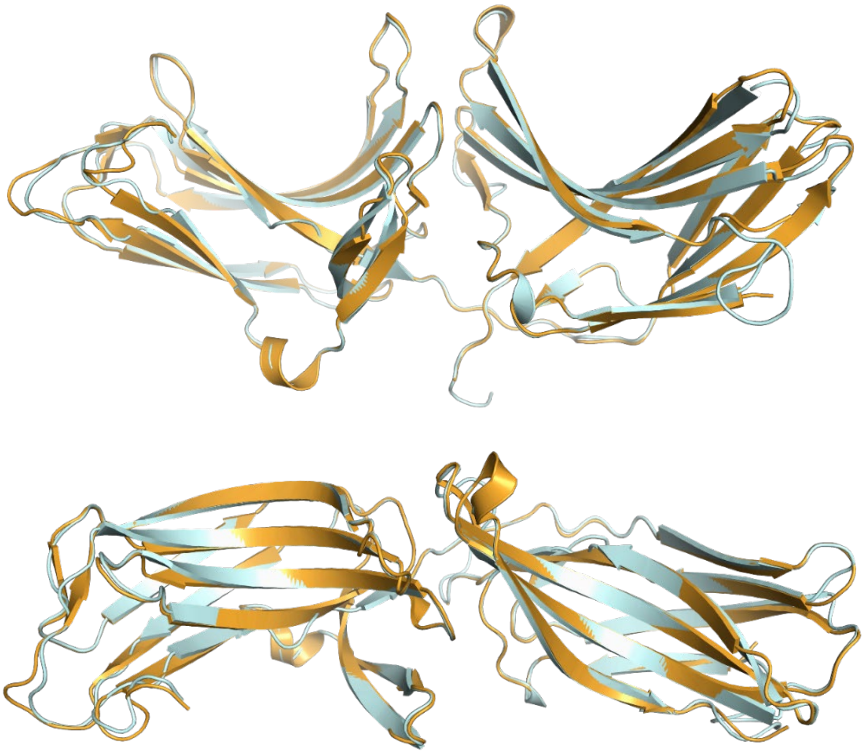

1772

1773

1774 F.

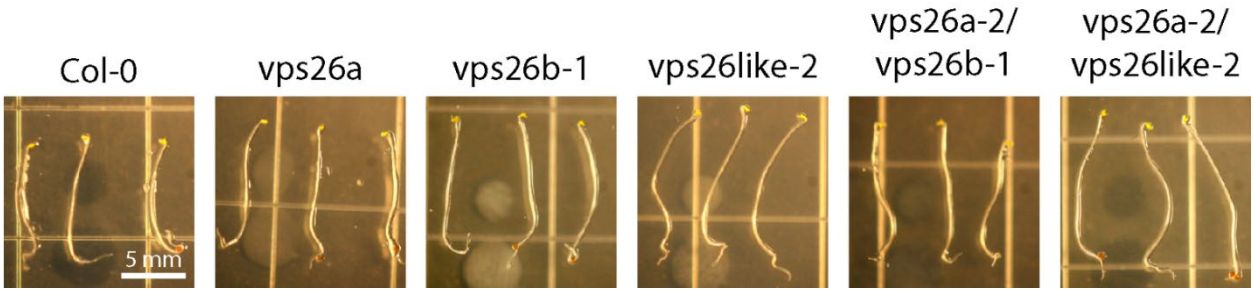

1775

Figure S5

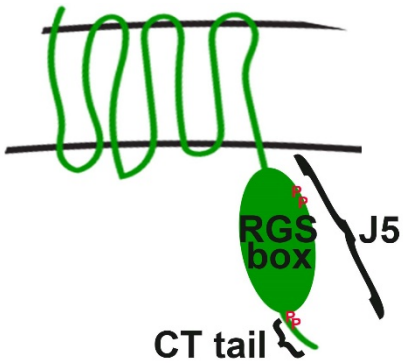

Figure S6

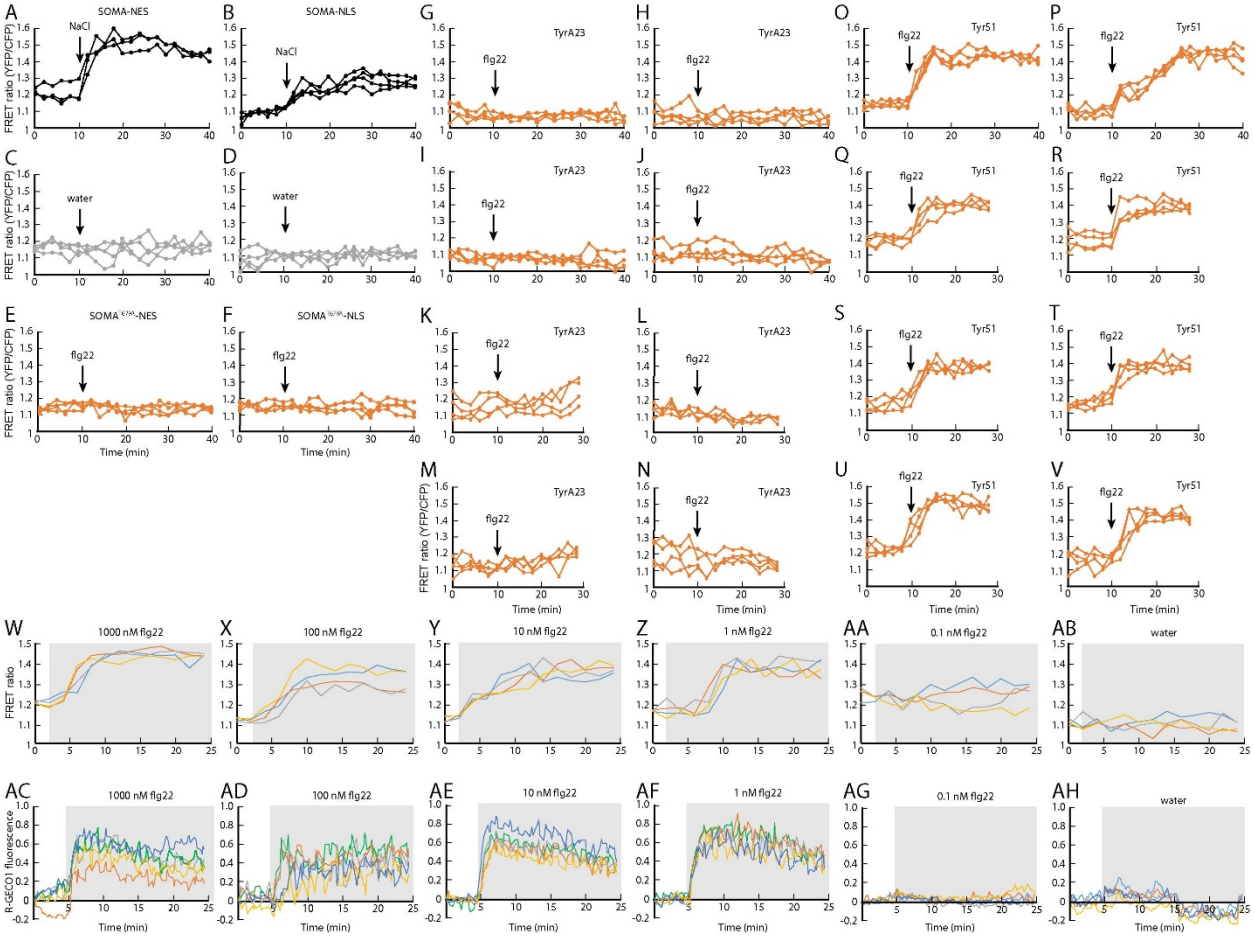

Supplemental code.

```
Data = xlsread('IMARIS statistics output')
% first step: sort the data based on the track ID, and
% subsort it on time points.
sortedData=sortrows(Data,[3,4]);
trackIDs=sortedData(:,3);
%trackIDs is only the ith column from the original sorted data, separate
%array
uniquetrackIDs=unique(trackIDs);
%uniquetrackIDs is a separate array with only unique track IDs

%StartEnd=zeros(length(uniquetrackIDs),2);
meanSpeedArea=zeros(length(uniquetrackIDs),2);

% Make a matrix with all its elements zeros. One dimension of the matrix
% is length of unique track IDs, i.e., the number of unique track IDs.
% Another dimension is 2 because we want to store the start and end
% locations of each of the unique track IDs.
for i = 1:length(uniquetrackIDs)
    ItrackID=uniquetrackIDs(i);
    locations=find(trackIDs==ItrackID);
    startLoc=locations(1);
    endLoc=locations(end);
    SpeedColumn=sortedData(:,1);
    meanSpeedArea(i,1)=mean(SpeedColumn(startLoc:endLoc));
    AreaColumn=sortedData(:,2);
    meanSpeedArea(i,2)=mean(AreaColumn(startLoc:endLoc));
    %StartEnd(i,1)=startLoc;
    %StartEnd(i,2)=endLoc;

end
```